Formation and coarsening of epitaxially-supported metal nanoclusters

Yong Han,[1,2] Da-Jiang Liu,[1] King C. Lai,[1,2,*] Patricia A. Thiel,[1,3,§] and James W. Evans[1,2]

[1]Ames National Laboratory USDOE, Ames, Iowa 50011
[2]Department of Physics & Astronomy, Iowa State University, Ames, Iowa 50011
[3]Department of Chemistry, Iowa State University, Ames, Iowa 50011

Abstract
This mini-review describes developments over the last ~30 years in characterizing the nucleation & growth of epitaxially-supported metal nanoclusters (NCs) or islands during vapor deposition, as well as their post-deposition coarsening. A beyond-mean-field treatment for homogeneous nucleation & growth corrects the deficiencies of traditional treatments in describing, e.g., the island size distribution, but also necessitates consideration of the spatial distribution of islands and their capture zones. We discuss advances in modeling capabilities, including those based upon on an ab-initio level treatment of periphery diffusion kinetics, for description of the non-equilibrium growth shapes of these NCs, mainly for 2D NCs. For post-deposition coarsening of arrays of NCs, there is generally a competition between Ostwald Ripening (OR) and Smoluchowski Ripening (SR). SR is also known as Particle Migration & Coalescence. For 2D NCs in homoepitaxial systems, conventional OR is observed on pristine fcc(111) surfaces, dramatically enhanced OR in the presence of even trace amounts of chalcogens for Cu(111) and Ag(111), and anomalous OR on anisotropic fcc(110) surfaces. The unexpected discovery of SR for fcc(100) homoepitaxial systems prompted extensive analysis of the underlying diffusivities of 2D NCs as a function of size, as well as of NC coalescence dynamics. A comprehensive understanding of these processes is now available. Self-assembly of 3D NCs during deposition, issues related to heterogeneous nucleation, directed assembly, and NC structure selection are addressed. For SR of 3D epitaxial NCs, shortcomings of the standard a mean-field treatment of the size-dependence of diffusivity are also revealed.

1. Introduction

In the first 30 years of surface science beginning in the 60's, studies of supported 3D metal nanoclusters (NCs) or "islands" formed by vapor deposition on non-metallic single-crystal substrates (alkali metal chlorides, graphite, oxides, etc.) effectively exploited Transmission Electron Microscopy (TEM) [1]. Real-scale images from TEM allowed characterization of individual NC growth morphologies, and also the distribution of NCs in size and space which resulted from the process of nucleation & growth (i.e., self-assembly) during deposition [1,2]. Post-deposition coarsening processes were also explored [1,2], where there was particular interest in coarsening pathways associated with the degradation of supported 3D metal NC catalysts [3]. A long-standing question was whether Ostwald Ripening (OR) or Smoluchowski Ripening (SR) [aka Particle Migration & Coalescence (PMC)] dominates. For these vapor deposition processes, there is generally a clear separation of time scales for NC formation during deposition and post-deposition coarsening (in contrast to analogous solution-phase processes). These early studies of NC formation prompted development of what we characterize as

mean-field (MF)-type theories for the homogeneous nucleation & growth of (either 2D or 3D) NCs by Zinsmeister, Venables, and others [4,5] which in particular describe the dependence of NC or island density on deposition flux, F, and surface temperature, T.

In the second 30 years, the ready availability of Scanning Tunneling Microscopy (STM) from the late 80's facilitated real-space imaging of epitaxial metal-on-metal systems in ultra-high vacuum where 2D NCs form due to strong adhesion of the deposited metal to the substrate [6-8]. In particular, studies of homoepitaxial systems focused on fundamental questions regarding film growth [9,10]. Analogous studies were performed for semiconductor systems, e.g., for Si/Si(100) [11]. These studies involved detailed investigation of far-from-equilibrium NC growth morphologies, and a quantitative assessment of self-assembly via homogeneous nucleation & growth (exploiting the feature that perfect that defect free surfaces can be prepared on a sufficiently large length scale, thus avoiding heterogeneous nucleation). Shortcomings of traditional MF nucleation theories in predicting the island size distribution (ISD) were revealed and explained [12,13] leading to development of beyond-MF treatments [10]. Post-deposition coarsening was also explored for homoepitaxy (again on a slower time scale than deposition) [14-16], where the unexpected dominance of SR for 2D islands rather than OR was found in some cases [17], and well as dramatic acceleration of OR in the presence of certain trace "additives" [18]. For these systems, a comprehensive understanding of behavior was often achieved by predictive atomistic-level stochastic modeling and Kinetic Monte Carlo (KMC) simulation capturing behavior on the appropriate time and length scales (in contrast to MD studies) [9,10]. These successes are highlighted in this contribution.

In the following, Sec. 2 reviews developments in homogeneous nucleation theory. Growth shapes formed during nucleation & growth of 2D metal-on-metal NCs are described in Sec. 3. Coarsening in 2D metal-on-metal NC systems is described in Sec. 4. In this contribution, the focus is on the case of 2D islands. However, in Sec. 5, we more discuss more briefly the formation and coarsening of 3D metal NCs on more weakly adhering supports. Conclusions are provided in Sec. 6.

2. Theory of homogeneous nucleation & growth during deposition

First, in **Figure 1**, we present a schematic highlighting the key features of self-assembly of supported NCs or islands via homogeneous nucleation & growth [10,19,20]. **Figure 1** is based on KMC simulation of the irreversible formation of near-square 2D NCs or islands, but the same basic features apply for 3D NCs. Desorption is assumed inactive corresponding to the regime of "complete condensation". The basic picture is that adatoms are deposited randomly on the surface, undergo rapid diffusive hopping across the surface, and aggregate into islands or NCs, which then grow by incorporation of subsequently deposited atoms. In the early "transient regime", the adatom density, N_1, builds up being roughly equal to the deposited coverage, θ. Once stable islands have nucleated, adatom depletion zones (DZ) grow about them (as each island periphery provides a sink for deposited diffusing adatoms). Subsequently, N_1 continues to increase while these DZs spread across the surface leading to their collision, which forms portions of so-called capture zone (CZ) boundaries. At the end of the transient regime, the DZs are transformed into a network of CZs which cover and tessellate the entire surface (with one island per CZ), and N_1 no longer increases. This

marks the onset of the steady-state regime where there is a rough balance between the gain of adatoms due to deposition, and the loss due primarily to capture by islands. It should be emphasized that nucleation of new islands continues, primarily close to CZ boundaries where the local N_1 is highest [19,20]. In fact, most islands are formed during the steady-state regime. CZs are so-named based on the picture that atoms deposited within a CZ are typically captured by the associated island within it.

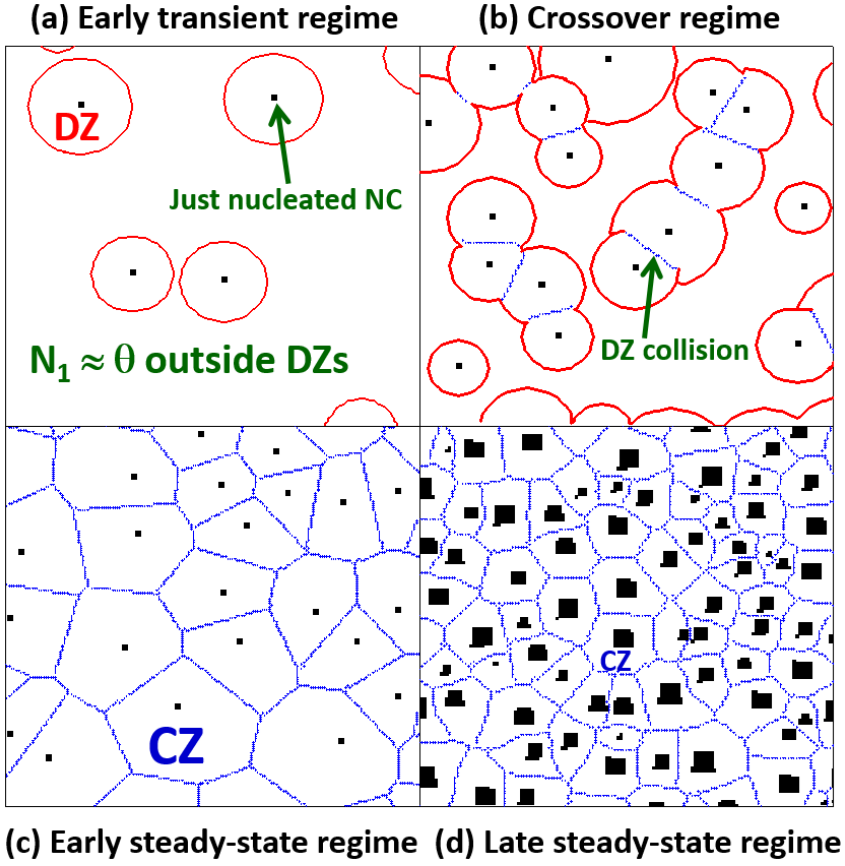

Figure 1. Schematic of homogeneous nucleation & growth (from simulations for irreversible formation of 2D square islands). Refined with permission from Ref. [10]. Copyright 2006 Elsevier.

2.1 Rate equations for the island density, N_{isl}, and adatom density, N_1

The density per adsorption site of NCs or islands of size s (in atoms) is denoted by N_s ($\leq$1). A critical size, i, is assigned such that islands with size s (in atoms) are stable only for s > i, so that the density of stable islands is given by $N_{isl} = \sum_{s>i} N_s$. Subcritical clusters with s $\leq$ i are locally equilibrated with the adatom density, yielding the Walton relation $N_i = \exp(-\beta E_i)(N_1)^i$ where $E_i < 0$ is the binding energy of a cluster of i atoms, and $\beta = 1/(k_B T)$ for surface temperature T and Boltzmann constant k_B. Below, F denotes the deposition flux (per adsorption site), and $h = \nu \exp(-\beta E_d)$ denotes the hop rate for terrace diffusion of adatoms with barrier E_d. The key parameter, h/F, is typically large given generally rapid surface diffusion. Note that the coverage satisfies $\theta = \sum_{s\geq 1} sN_s = Ft$ for deposition time t. For nucleation rate, K_{nuc}, and rate of aggregation with stable islands, K_{agg}, one has that [4,10]

$$d/dt\ N_1 = b(\theta)F - K_{agg} - (i+1)K_{nuc} \text{ and } d/dt\ N_{isl} = K_{nuc}, \quad (1)$$

where $K_{nuc} = \sigma_i\, h\, N_1\, N_i$ and $K_{agg} = \sigma_{isl}\, h\, N_1\, N_{isl}$, and σ_{isl} (σ_i) denotes the "capture number" for stable islands (for critical clusters of size i). Also $b(\theta)$ denotes the bare fraction of the substrate not covered by islands at coverage θ (so that $b(\theta) = 1 - \theta$ for 2D islands), but below for simplicity we set $b(\theta) \approx 1$. Early transient regime behavior, $N_{isl} \sim \theta^{i+2} \exp(-\beta E_i)(h/F)$, follows immediately using $N_1 \approx \theta$. Steady-state behavior follows from using the relation $F \approx K_{agg}$, and yields the central result of nucleation theory

$$N_{isl} \sim \theta^{1/(i+2)} \exp[-\beta E_i/(i+2)](h/F)^{-\chi} \text{ with scaling exponent } \chi = i/(i+2). \quad (2)$$

Thus, if $N_{isl} \sim \exp(-\beta E_{eff})$, one has that $E_{eff} = (i\,E_d + E_i)/(i+2)$. Matching expressions for N_{isl} in the transient and steady-state regimes shows that crossover occurs for very low coverages $\theta = \theta^* \approx \exp[\beta E_i/(i+3)](h/F)^{-2/(i+3)}$. Another quantity of basic interest is the mean island size, $s_{av} = \theta/N_{isl}$, which is readily obtained from N_{isl}.

A schematic summary of the behavior of N_{isl} and N_1 is provided in **Figure 2**. The coverage scaling in (2) is significantly modified above low θ by effects of finite island extent. The variation with h/F or with T is invaluable to extract information on critical size and the underlying energetics. Some refinement to the above formulation is required for strongly anisotropic surface diffusion [12] (revising [11]), or if smaller stable clusters have significant mobility [10]. For example, if i = 1 (irreversible island formation), but there is significant dimer mobility with hop rate h′, then one has that $N_{isl} \sim (h h'/F^2)^{1/5}$ [9,10].

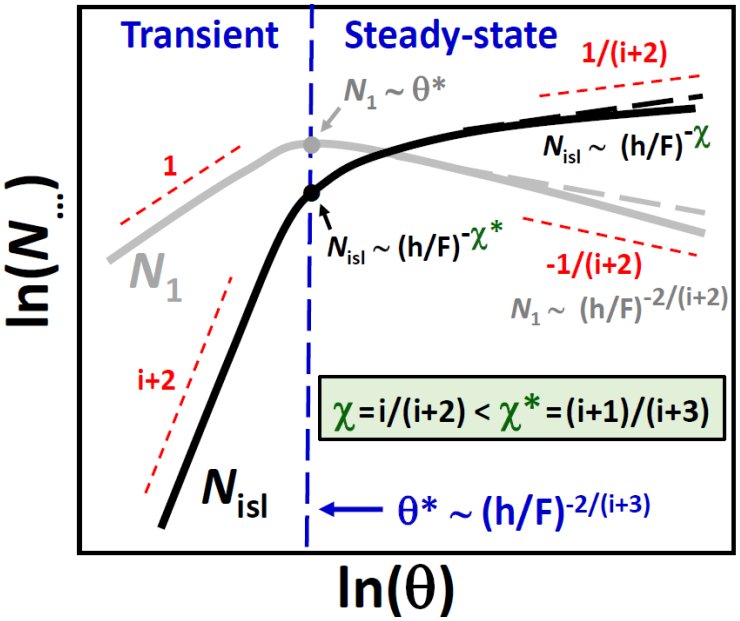

Figure 2. Schematic behavior of N_{isl} and N_1 where the figure is geared to smaller i (as for bigger i, N_1 can dominate N_{isl} in the steady-state). Slopes on this log-log plot are indicated in red. Boltzmann factors involving E_i are ignored. Deviation from simple θ-scaling behavior (dashed lines) in the steady state is due to finite island extent. See [10] for corresponding plots based upon data from KMC simulations.

It remains to assign the critical size, i, which should increase with T. Traditionally, this is done by adapting the concepts of Classical Nucleation Theory (CNT) [21]. Assuming local equilibration of all subcritical clusters with the adatom density (which itself is determined by the deposition process), one as that $N_s \approx \exp(-\beta E_s)(N_1)^s$ for $s \leq i$, where $E_s < 0$ is the binding energy for a cluster of size s. The critical size corresponds to the minimum N_s [4,5]. For 2D epitaxial clusters on isotropic surfaces where $\phi > 0$ is the effective nearest-neighbor (NN) bond strength, a reasonable approximation is that $E_s = -M_s \phi$ so $N_s \approx \exp(\beta M_s \phi)(N_1)^s$ where M_s is the number of NN bonds in the lowest energy ground-state configuration of a cluster of s atoms. Thus, one has that $M_1 = 0$ for an adatom, $M_2 = 1$ for a dimer, but $M_{s>2}$ depend on epitaxial geometry. See **Table I**. For low-T, the increase in the Boltzmann factor in N_s will dominate the decrease in $(N_1)^s$ with increasing s, so that $N_1 \leq N_{s>1}$ and i = 1 (irreversible island formation). The transition to reversible island formation with i > 1 occurs when T increases sufficiently so that N_2 decreases to equal N_1 [i.e., when $N_1 = \exp(-\beta\phi)$]. More detailed analysis reveals that for {100} epitaxy, there is a transition directly from i = 1 (stable dimers) to i = 3 (stable square tetramers), and for {111} epitaxy from i = 1 (stable dimers) to i = 2 (stable triangular trimers) and then to i = 6 (stable hexagonal heptamers). See the supplementary materials (**SM**). More generally, this approach is traditionally used to map out regimes of i versus T [4,5].

Table I. Number of NN bonds, M_s, for clusters of size s atoms for fcc {100} and {111} epitaxy. In some cases, cluster shapes are indicated (e.g., a square tetramer for fcc(100) when s = 4).

fcc(100)	$M_1 = 0$	$M_2 = 1$	$M_3 = 2$ ∟,--	$M_4 = 4$ □	$M_5 = 5$	$M_6 = 7$	$M_7 = 8$
fcc(111)	$M_1 = 0$	$M_2 = 1$	$M_3 = 3$ Δ	$M_4 = 5$ ◊	$M_5 = 7$	$M_6 = 9$	$M_7 = 12$

More recently, an alternative (but equivalent) kinetic formulation has been utilized producing “practical criterion” for the transition from i = 1 to i > 1 [22]. Here, the focus is on the relative magnitude of the aggregation rate of monomers with each dimer, $K_{agg} \sim \sigma_2 h N_1$, and the rate of dissociation of each dimers, $K_{diss} \sim h \exp(-\beta\phi)$. The regime i = 1 corresponds to $K_{agg} > K_{diss}$, i.e., dimers are stable on the time scale of aggregation, and the transition (starts to) occur when these rates are roughly equal. This criterion matches that above (if one neglects the capture number, or if one implements a more rigorous formulation which uses detailed-balance to show that the effective K_{diss} also involves a factor of σ_2 [23]). Thus, a natural parameter tracking the crossover from i = 1 to i > 1 is the ratio $R_{d/a} = K_{diss}/K_{agg}$. Using the steady-state relation to express N_1 in terms in N_{isl}, one finds that

$$R_{d/a} \sim Y^{2/3} \text{ where } Y = (\nu/F) \exp[-\beta(E_d + 3/2\ \phi)]. \quad (3)$$

Thus, Y provides a practical crossover-variable where the onset of reversible island formation occurs for $Y \approx 1$ - 10. However, contrasting the traditional picture of sharp transitions in critical size, there is a broad transition regime beyond i= 1 before one finds a regime corresponding (it seems only for a narrow window of Y) to i = 3 for {100} epitaxy [22,24,25]. See **Figure 3**. Analogous behavior applies for the transition from i = 1 to i = 2 for {111} epitaxy [26,27]. As a further illustration of the utility of (3), in **Table II**,

we provide corresponding estimates of the temperature, T_{rev}, associated with the onset of the transition to reversible island formation for various metal homoepitaxial systems.

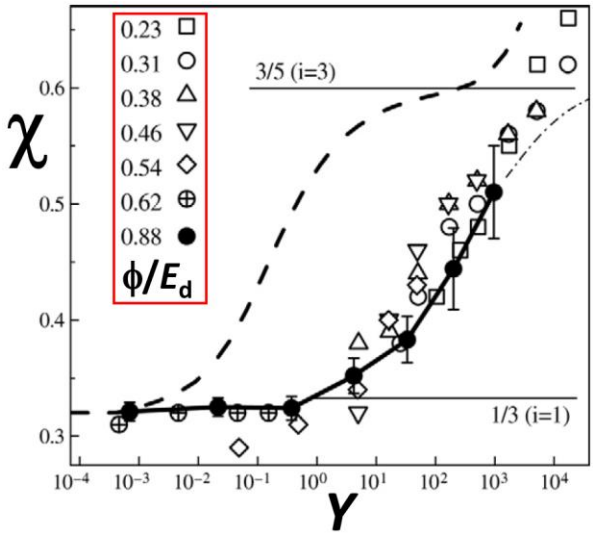

Figure 3. Variation of the scaling exponent, χ, for the island density as a function of the crossover parameter Y for the transition from irreversible island formation i = 1 to i = 3 for {100} epitaxy. Recall that nominally $\chi = i/(i+2)$. Results are shown from KMC simulation in [24] (closed symbols) and [25] (open symbols), and from a simple MF treatment [22]. The existence of a substantial well-defined regime with i = 3 is not so evident from (precise) KMC simulation. Refined with permission from Ref. [10]. Copyright 2006 Elsevier.

Table II. Estimates of T_{rev} for the transition to reversible island formation in metal homoepitaxy based upon $Y = 10$ choosing F = 0.01 ML/s and $\nu = 10^{12.5}$/s, so that $T_{rev} = 373.3(E_d + 3\phi/2)$. *An estimate of the onset temperature, T_{mob}, where dimer mobility impacts N_{isl} comes from replacing $\phi/2$ in T_{rev} by $E_d' - E_d$, where E_d' is the barrier for dimer mobility [10]. Thus, the relevant case $T_{mob} < T_{rev}$ applies when $E_d' - E_d < \phi/2$ which applies for Pt(111) with $E_d' \approx 0.37$ eV so $T_{mob} \sim 220$ K.

	Ag(100)	Ag(111)	Cu(100)	Cu(111)	Pt(111)*	Fe(100)
E_d, ϕ (in eV)	0.45, 0.26	0.08, 0.22	0.48, 0.33	0.05, 0.27	0.26, 0.63	0.45, 0.50
T_{rev}	315 K	150 K	365 K	170 K	445 K	450 K

2.2 Rate equations for the island size distribution (ISD): N_s vs s

The evolution of the density, N_s, of stable islands of size s > i satisfy standard Becker-Doering type population dynamics equations

$$d/dt\ N_s = h\ \sigma_{s-1}\ N_1\ N_{s-1} - h\ \sigma_s\ N_1\ N_s \quad \ldots \text{ for } s > i. \qquad (4)$$

where σ_s denotes the capture number for islands of size s. These are supplemented for the Walton relation for N_i and the above equation for N_1. Clearly, the form of N_s versus s will depend on the s-dependence of σ_s. Most interest is in the scaling regime of large h/F and large s_{av}, where one anticipates scaling form

$N_s \approx (N_{isl}/s_{av})\ f(x)$ where $x = s/s_{av}$ with $\int dx\ f = \int dx\ x\ f = 1$, (5)

neglecting any θ-dependence of *f*. Also adopting a scaling form for $\sigma_s = \sigma_{isl}\ C(x)$ [28], and neglect θ-dependence of *C*, then one obtains the exact relation [10]

$f(x) = f(0)\ \exp[\int_{0<y<x} [(2z-1) - dC(y)/dy]/[C(y) - zy]$, (6)

where $s_{av} \sim \theta^z$ and z = (i+1)/(i+2) for low θ (with deviations for larger θ).

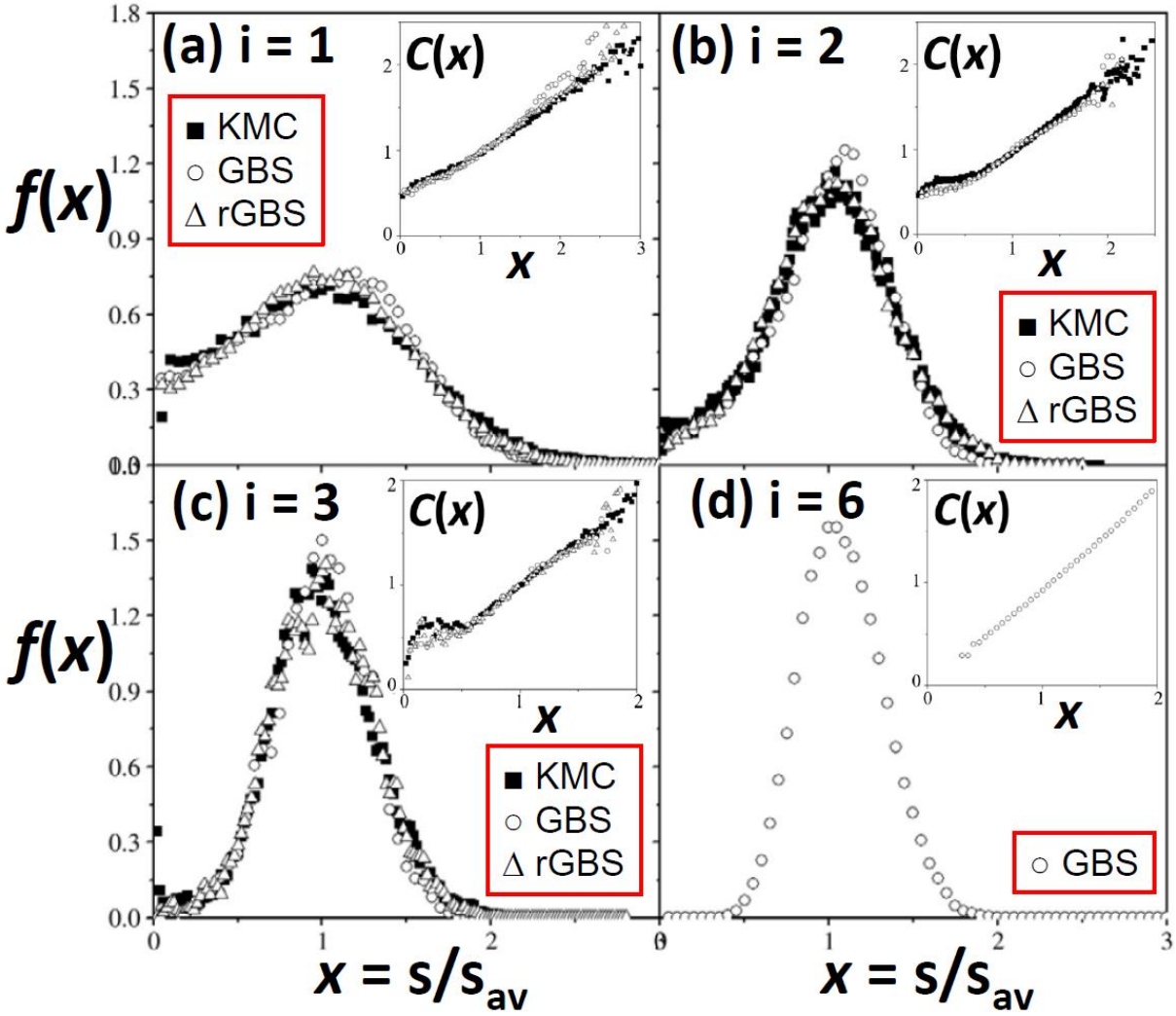

Figure 4. Scaling functions, *f*(x), for the ISD obtained for 2D compact islands. Insets show scaling functions, *C*(x) = a(x), for the capture number (or CZ area) versus island size. KMC results are compared with those from standard and refined Geometry-Based Simulation. Refined with permission from Ref. [20]. Copyright 2003 Elsevier.

The form of the scaling function *C*(x) for capture numbers is required to explicitly evaluate *f*(x). *C*(x) has contributions from direct deposition on top of the islands, and from diffusive aggregation, but we emphasize the latter here. Traditional MF treatments

took considerable care to develop of self-consistent evaluation of σ_s versus s solving an appropriate deposition-diffusion equation for the capture of deposited atoms accounting for the mean environment of the "island sink". The corresponding $C(x)$ initially increases quickly like $1/|\ln(x)|$ as x increases above zero, but then sub-linearly roughly like $x^{1/2}$ for larger x. This results in a divergence of $f(x)$ at $x = x_s$ where $C(x_s) = zx_s$, and where $f(x) \equiv 0$ for $x > x_s$. For finite h/F, this singularity is smoothed out. However, the fundamental flaw in this MF treatment is the neglect of a significant non-MF dependence of the local environment of islands on their size. Specifically, KMC simulation and experimental analysis shows that larger islands are more distant from their neighbors. As a result, $C(x)$ increases quasi-linearly for with x, and the singularity in (5) is averted. This non-MF form of $C(x)$ is confirmed not just by KMC simulation [10,13,19,20], but also by analysis of experimental data [26,27]. Examples of scaling functions, $f(x)$, and the corresponding $C(x)$ are shown in **Figure 4** for models with prescribed critical size i = 1, 2, 3, and 6. Note that the scaled ISD $s_{av} N_s/N_{isl}$ versus s/s_{av} produce a family of curves with higher peaks and lower left shoulders for increasing h/F, and where strictly (5) corresponds to limiting behavior for $h/F \rightarrow \infty$. Finally, it should be emphasized that (4-6) do not provide a complete beyond-MF theory of the ISD, as they do not provide the form of $C(x)$. For a more complete theory, see Sec. 2.5.

A key feature of the ISD is that $f(0) > 0$ most clearly for small critical sizes. This is also reflected in the relation $C(0)\, f(0) = 1\text{-}z$ [13]. In contrast, a popular form of Amar & Family [31] for $f(x) \sim x^i \exp(-ia_i\, x^{1/ai})$, where a_i is determined by $\int dx\, x\, f = 1$, sets $f(0) = 0$. Their simulations for i =1 involved fractal islands with fixed θ which suppressed $f(x)$ for small x relative to compact islands. Also, there is often a delay between experimental imaging and the end of deposition during which the higher mobility of small clusters which aggregate with larger clusters can suppress $f(x)$ for small x [32].

The availability of precise experimental ISD data is limited even for metal homoepitaxy, although data does exist for Fe/Fe(100) and Ag/Ag(100) [10]. For the latter, mobility of small clusters after deposition and before imaging does deplete the population of small islands relative to theory predictions in Sec. 2.

2.3. Exact and approximate Capture Zones (CZ)

First, we elaborate further on the concept of CZs illustrated in **Figure 1** where atoms deposited within a CZ are typically captured by the associated island. The basic concept was advanced in the earlier literature [33,34]. In principle, capture zones can be constructed so that the rate of growth of an island is exactly equal to the deposition flux times the CZ area. This is achieved by solving the steady-state deposition-diffusion equation for the island and those in its vicinity with zero adatom density at island edges which act as "sinks". This allows determination of the field lines for the surface diffusion flux, and following these from all points within the CZ lead to the associated island. See **Figure 5a**. In fact, exact CZs can well-approximated from a simpler Voronoi-type construction where CZ boundaries are equidistant from nearby island edges. See **Figure 5b**. See Ref. [29,30]. In addition, in the context of ISD analysis, it is instructive to let A_s denote the mean CZ area for islands of size s. Then, for the exact CZs, it follows that the rate of aggregation with islands of size s is given by $h\, N_1\, \sigma_s = F\, A_s$ [which can be used to recast (4)]. Then the scaling function for capture numbers and these CZ

areas coincide, i.e., $A_s = A_{av}$ a(x), where $A_{av} = 1/N_{isl}$, then a(x) = C(x). Thus, C(x) can be determined from a CZ area analysis.

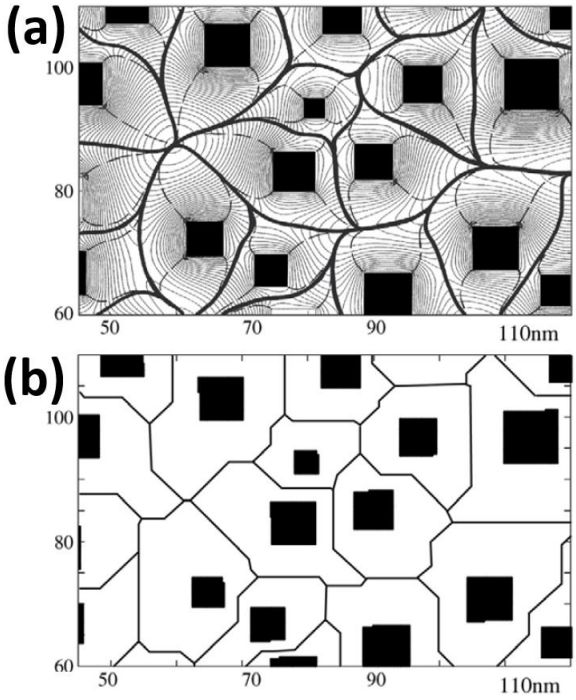

Figure 5. Capture zones for Ag islands on Ag(100) with the island distribution extracted from STM [30]: (a) exact analysis; (b) modified Voronoi construction. Note that for the exact CZs in (a), contours of equal steady-state adatom density are shown, and CZs are also decomposed into sub-CZs for each island edge (see dashed lines). Refined with permission from Ref. [30]. Copyright 1999 American Physical Society.

2.4. Capture Zone area Distribution (CZD): N_A vs A

From the 60's through the 90's, there was considerable focus on analysis of the ISD. However, subsequently interest developed in detailed characterization of the capture zone (area) distribution (CZD), N_A, versus A, where N_A is the density of islands with CZ area A, so that $N_{isl} = \sum_A N_A$. Thus, one anticipates a scaling form

$$N_A \approx (N_{isl}/A_{av})\, g(\alpha) \text{ where } \alpha = A/A_{av} \text{ with } \int d\alpha\, g = \int d\alpha\, \alpha g = 1, \qquad (7)$$

neglecting any θ-dependence of g. A heuristic formulation [35] of N_A suggested a Gaussian tail for large A, and that behavior for small A was controlled by the critical size for nucleation, where the latter specific prediction was later corrected [36,37]. Our perspective was to develop a theory for N_A based upon the fundamental exact evolution equation which is represented schematically in **Figure 6**. The population, N_A, can increase if a new CZ is formed with area A, or if creation of a new CZ by nucleation nearby and thus overlapping with an existing CZ with area larger than A reduced its area to A. The population N_A can decrease if nucleation nearby a CZ of area of A creates a new overlapping CZ thus reducing the area of the existing CZ below A. See

the 3rd, 2nd, and 1st terms in **Figure 6**, respectively. Thus, it is clear that rigorous analysis of N_A requires characterization of the finer details of nucleation, the absence of which precludes complete analysis. Some relevant quantities are the mean number, $M_0 \approx$ 4-5, of existing CZ's overlapped by a new CZ. Also, if a new CZ overlaps an existing CZ, the mean fraction of area overlapped is $\mu_{av} \approx 0.1$ at 0.1 ML [36,37].

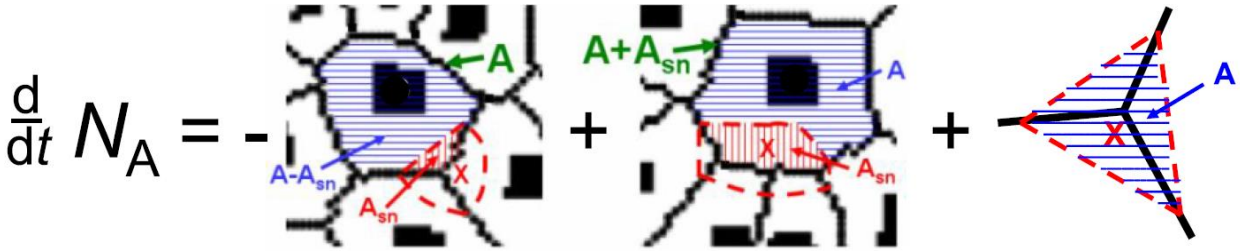

Figure 6. Schematic for evolution of the population, N_A, of islands with CZ area A. Refined with permission from Ref. [37]. Copyright 2016 American Institute of Physics.

Even without a complete analysis for N_A or $g(\alpha)$, one can however provide insight into behavior for small A or α. Let $P^*(A)$ denote the probability of nucleation a new CZ of area A, where we naturally adopt the scaling form $P^*(A) = (A_{av})^{-1} p^*(\alpha)$ with $\int d\alpha\, p^* = 1$. For small A, we first assume that the 3rd term in **Figure 6** which is given by $P^* dN_{isl}/dt$, dominates, so that [36,37]

$$d/dt\, N_A \approx P^*(A)\, dN_{isl}/dt \;\text{ yielding }\; 2g(\alpha) + \alpha\, dg(\alpha)/d\alpha \approx p^*(\alpha). \qquad (8)$$

Adopting the form $g(\alpha) \sim \alpha^\beta$ for small α, it follows that $g(\alpha) \approx (2+\beta)^{-1} p^*(\alpha)$, i.e., the form of $g(\alpha)$ is directly determined from that for $p^*(\alpha)$ for small α. We first focus on the scenario where small CZs can be formed by nucleation along a CZ boundary between pairs of existing nearby islands of finite extent, neither of which need have a small CZ. See **Figure 7a**. (A small CZ also results from nucleation within group of three or more nearby islands, but with lower probability.) Let $r_{isl} \sim (A_{av})^{1/2}$ measure the mean separation between islands. Then, the separation, r, of nearby islands associated with the formation of CZs with small α scales like $r/r_{isl} \sim \alpha^{1/2}$. Evaluation of $p^* = p_{pair}\, p_{nuc}$ must account for both the relative probability of finding a nearby pair of islands, $p_{pair} \sim (r/r_{isl})^{i+2}$, and the relative probability of nucleation in the small confined space between islands, $p_{nuc} \sim (r/r_{isl})^{2i+4}$. See the **SM** for details. Since $g(\alpha) \sim p^*(\alpha)$, one obtains

$$g(\alpha) \sim \alpha^\beta \text{ with } \beta = 3i/2 + 3. \qquad (9)$$

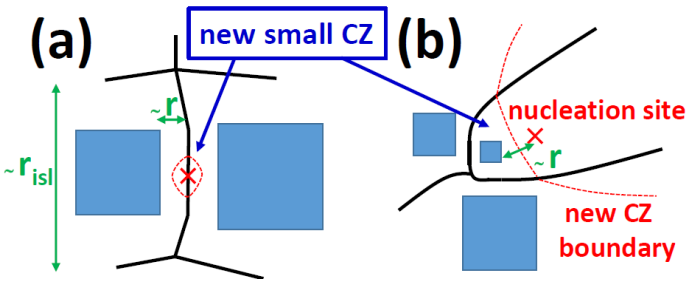

Figure 7. Schematics for the formation of CZs with small area $A << A_{isl}$ or $\alpha << 1$.

A second scenario to create small CZ is shown in **Figure 7b**. This corresponds to the second term in **Figure 6** (contrasting the above assumption that the third term dominates). Here, one starts with a nearby triple of islands, none of which necessarily has a small CZ. The probability of this configuration scales like $p_{triple} \sim (r/r_{isl})^{2i+3}$ [37]. In addition, a fourth island must nucleate a distance $r << r_{isl}$ from one of these converting its large CZ into a small CZ. This nucleation probability is $p_{nuc^*} \sim (r/r_{isl})^{i+3}$ which differs from p_{nuc} as here nucleation does not occur in a confined space between nearby islands [37]. See the **SM**. Using that $g(\alpha) \sim p_{triple}\, p_{nuc^*}$, one actually recovers (9). While there remains some uncertainty in this analysis of β, it seems to agree reasonably with simulation results (see below).

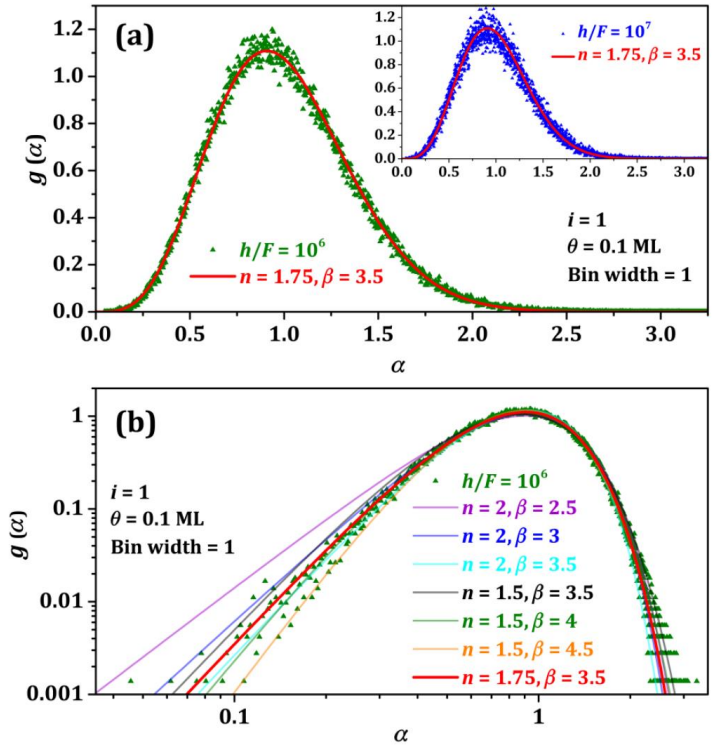

Figure 8. KMC simulation results for the scaled CZ area distribution, $g(\alpha)$, versus $\alpha = A/A_{av}$ for 2D square islands with i = 1. Data is fit to a GG distribution, $g_{GG}(\alpha) \approx a\, \alpha^{\beta} \exp(-b\alpha^{n})$. Refined with permission from Ref. [37]. Copyright 2016 American Institute of Physics.

Simulation data for $g(\alpha)$ is typically fit with a generalized gamma (GG) distribution, $g_{GG}(\alpha) \approx a\, \alpha^{\beta} \exp(-b\alpha^{n})$, where a and b are determined in terms of β and n from $\int d\alpha\, g = \int d\alpha\, \alpha g = 1$. (We emphasize that this is a just convenient form with the flexibility to capture a variety of behavior for both small and large α, but it should not correspond precisely to the solution of the exact evolution equation for N_A.) **Figure 8** shows results for 2D square islands with i = 1 at θ = 0.1 ML where the best fits are compatible with β = 3.5-4. Similar analysis for i = 0 (corresponding to mobile adatoms converting at a fixed rate immobile seeds for nucleation as suggested for Fe/Cu(100) [38]), best fits are compatible with β = 2.75-3 [37]. Thus, there is reasonable agreement with the above theory, although some uncertainty remains [39]. It seems reasonable to

rule out early predictions of $\beta = i + 1$ or $i + 2$ [35,40]. A key driver of this theory for the CZD [35] is the potential to extract the critical size from experimental CZD data, although there are practical issues with limited data for small α. Another issue is the prediction of a Gaussian tail to $g(\alpha)$ for large α [35]. This is plausibly compatible with the simulation data in **Figure 8** [37]. One simulation study questioned the existence of a Gaussian tail for large α [39], whereas another suggested its existence except for small *h/F* [41]. Distinct behavior for low *h/F* is reasonable as when $h = 0$ for low coverages, CZs correspond to a standard Poisson-Voronoi tessellation where the area distribution for large sizes exhibits exponential decay [42].

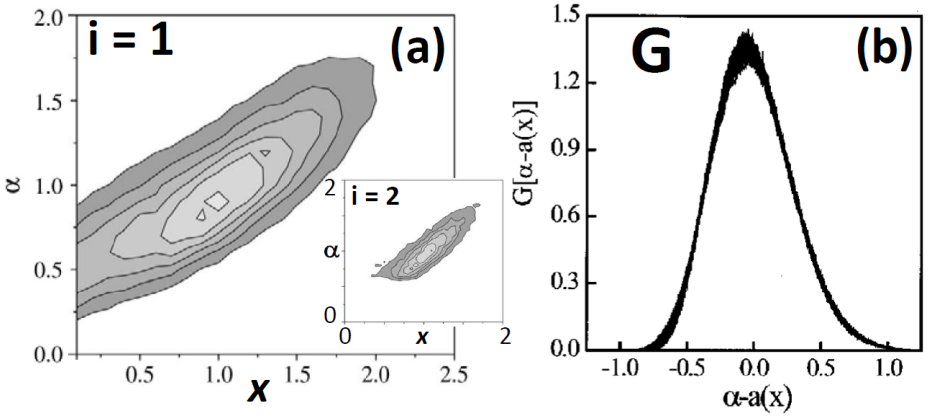

Figure 9. KMC simulation results for: (a) the scaling function $F(x, \alpha)$ for the JPD for island sizes and CZ areas for i = 1 (and for i = 2 in the inset, but where limited data cannot capture the finite population for smaller sizes); (b) the scaling function $G[\alpha - a(x)] = F(x, \alpha)/f(x)$ for JPD factorization when i = 1. (a) Refined with permission from Ref. [20]. Copyright 2003 Elsevier. (b) Reprinted with permission from Ref. [45]. Copyright 2002 American Institute of Physics.

2.5 Joint Probability Distribution (JPD) for NC size and CZ area: $N_{s,A}$

The above analysis reveals that the island size distribution is determined by the size-dependence of capture numbers which corresponds to that of the CZ area on size. This suggests that a comprehensive theory of nucleation & growth should be based on analysis of the joint probability distribution (JPD), $N_{s,A}$, of island sizes, s, and CZ areas, *A*. The initial such study by Mulheran & Robbie [43] constituted a significant conceptual advance. With $x = s/s_{av}$ and $\alpha = A/A_{av}$ as above, one anticipates a scaling form

$$N_{s,A} \approx \{N_{isl}/(s_{av} A_{av})\} F(x, \alpha) \text{ where } \int dx \int d\alpha\, x^i \alpha^j F = 1 \text{ for i or j = 0 or 1.} \quad (10)$$

In addition, one has that $f(x) = \int d\alpha\, F$, $g(\alpha) = \int dx\, F$, and $f(x)a(x) = \int d\alpha\, \alpha\, F$ where $\int dx\, f(x)a(x) = 1$. In principle, one can develop exact evolution equations for $N_{s,A}$ [44,45]. However, these require as input a detailed characterization of the nucleation process including the probability that nucleation of a new island which creates a new CZ impacts an existing CZ or area *A* associated with an island of size s, and the fraction of the CZ area which is overlapped by the new CZ (which in part reflects the mean number $M_0 \approx$ 4-5 of existing CZs overlapped by the new CZ). Initial studies assumed that nucleation just fragmented an existing CZ into two (i.e. $M_0 = 1$) [43], and a later study assumed all new CZs have the average area, and ignored the impact of nucleation on existing CZs

[46]. An effort has been made to incorporate a realistic treatment of nucleation [44,45], which does lead to reasonable predictions for the ISD, and for the key scaling function a(x), but a satisfactory complete theory remains an open challenge. In **Figure 9**, we just show results for the JPD from KMC simulation for i = 1 and i =2, which support a factorization relation, $F(x, \alpha) = G[\alpha - a(x)]\, f(x)$ [45].

2.6 Simulation approaches

In KMC simulation of stochastic lattice-gas (LG) models, atoms reside at a periodic array of epitaxial adsorption sites, and various processes (deposition, terrace diffusion, periphery diffusion) are implemented with probabilities proportional to their physical rates. At least for small critical sizes, i, KMC incorporating a rejection-free Bortz type algorithm [47] can handle large variations in rates (e.g., h/F exceeds 10^7 for Ag(100) homoepitaxy with F = 0.01 ML/s at room temperature, and is far higher for Ag(111) homoepitaxy). While adatoms undergoing terrace diffusion hop rapidly, there are few of them recalling that $N_1 \sim (h/F)^{-2/(i+2)}$, so total rates for deposition and hopping are not as different as might be expected. However, for larger critical size and a large population of rapidly hopping terrace adatoms, direct KMC simulation is not viable. To illustrate this issue, **Table II**, reports the how the CPU time, τ_i, increases with critical size i for simulation with $h/F = 10^6$ up to θ = 0.1-0.2 ML [48].

Table II. Dependence of simulation time τ_i on critical size i for $h/F = 10^6$.

τ_2/τ_1	τ_3/τ_2	τ_4/τ_3	τ_5/τ_4
~ 32	~19	~8	~5.5

To address this challenge particularly for large i, hybrid approaches might be considered which treat the terrace diffusion in a continuum (or other more efficient) formalism, but retain an atomistic treatment of island structure. One quasi-continuum KMC (QCMC) approach solved the continuum deposition-diffusion equation but used the input to stochastically attach/detach adatoms from islands, thus correctly retaining fluctuations and potential shape instability in island growth (see Sec. 3) [49]. Another approach enhanced simulation efficiency by coarse-graining the hopping dynamics in terrace diffusion [50]. Yet another strategy adopted a fully continuum level-set treatment for 2D islands. The level set is a continuum field evolved by a partial differential equation (PDE) where its contours at a specific threshold value corresponds to periphery of the islands [51], and this PDE is coupled to the continuum deposition-diffusion equation. There is, however, a challenge in capturing island growth shapes as discretization of the PDEs artificially smooths the periphery, edge diffusion was often neglected, and in any case the appropriate form for non-equilibrium edge diffusion flux (which differs from the standard Mullins quasi-equilibrium flux) is not so clear [10].

One other approach, termed (stochastic) Geometry Based Simulation (GBS) [19,20], has been particularly effective in allowing, e.g., efficient determination of the ISD for larger critical size, i. The physically motivated GBS approach is based upon the picture in **Figure 1**. The main features are as follows: (i) islands are simply grown at a rate determined by the area of their CZs; (ii) new islands are nucleated near the boundaries of the CZs where the local adatom density, and thus the nucleation rate, is highest. An appropriate approximate analytic treatment determines the value of this

nucleation rate, and its variation along the CZ boundaries. The simplest treatment implementing nucleation right on the CZ boundaries fails to accurately capture the pair distribution function for islands, but this deficiency is resolved in a refined treatment (rGBS) allowing some deviation in nucleation locations from the CZ boundaries. **Figure 4** shows results from GBS simulation for the ISD matching those from KMC simulation.

3. 2D epitaxial metal-on-metal NCs: Growth shapes and structures

In this section, we focus on the growth shapes and structure of individual NCs or islands during deposition, and shape transitions with varying deposition *T*. We compare STM and KMC results. As is generally the case for self-assembly of NCs [52], during the growth of NCs or islands during deposition, growth shapes are determined by a competition between aggregation (which produces a DLA or Mullins-Sekerka type shape instability in the case of diffusion-mediated growth) and relaxation or restructuring of atoms within the aggregate (in our case primarily via edge or periphery diffusion). The relative magnitude of growth and relaxation rates will determine how far growth shapes deviate from equilibrium forms. From Sec.2, it is clear that the growth rate is simply determined by the CZ area (and *F*). Thus, the main challenge is to precisely describe the rates for relaxation, i.e., periphery diffusion rates for a diversity of local step edge environments, and intermixing rates for multicomponent NCs.

However, digressing briefly from this main theme, we emphasize that the homogeneous nucleation & growth process, particularly for 2D epitaxial metal NCs on defect-free single-component crystalline substrates, is captured precisely by the concepts of Sec. 2. Multiple experimental studies for such systems have explored the transition from i = 1 to reversible island formation (or to a regime with significant dimer mobility) [9,10]. It is appropriate to note at least some indirect connection between the nucleation process and island structure focusing on metal{111} epitaxy (with rapid terrace diffusion and inhibited periphery diffusion) where island shapes tend to exhibit a fractal or dendritic shape instability at low *T*. Certainly for i = 1, this shape instability can be manifested. However, even for i = 2 where triangular trimers but not dimers are stable, this should be possible. Why? A barrier of $E_d + \phi$ must be surmounted for reversible island formation (see Sec. 2). However, to quench the shape instability, not only is it necessary for diffusion along straight close-packed step edges to be operative, but also kink or corner rounding [53]. The barrier for latter is generally expected to exceed $E_d + \phi$. However, for i >2, a barrier of $E_d + 2\phi$ must be surmounted which is likely higher than that for kink rounding. Thus, in the regime of i > 2, one does not anticipate fractal or dendritic islands. Finally, we also note some influence of growth shape on the local environment of island, at least for inhibited periphery diffusion. This is perhaps most clearly reflected in a decomposition of CZs for 2D polygonal islands into sub-CZs associated with individual edges, where those edges with the largest sub-CZs will grow fastest introducing a directionality into island growth [29,30].

3.1. Predictive modeling of growth shapes and structures

Generic prescriptions of periphery diffusion barriers (Initial Value Approximation or bond-breaking, symmetric Brønsted-Evans-Polyani, etc.) fail for metal systems [10,54]. Earlier successful modeling for specific systems tended to build simple tailored

models geared to capture the key features of periphery diffusion for those systems, or through incorporation “by hand” of appropriate values for key periphery diffusion processes [9,10]. Recent efforts have exploited what may be termed an Unconventional Interaction – Conventional Interaction (UICI) formalism [54-56]. This approach exploits the feature that the activation barrier for hopping has the form, $E_{act} = E_{TS} - E_{init}$, where E_{init} is the energy associated with the hopping atom in its initial adsorption site, and E_{TS} is the energy in the transition state between initial and final adsorption sites. For 2D epitaxial NCs, E_{init} can be determined by conventional lateral interactions between adatoms at adsorption sites, familiar from equilibrium lattice-gas models. These interactions can be decomposed via a cluster expansion into pair, triplet, etc., components. E_{TS} is determined from unconventional (pair, triplet, etc.) lateral interactions, between the hopping atom at the transition state and nearby atoms at epitaxial adsorption sites (e.g., for a bridge site TS and hollow adsorption sites). E_{TS} also includes an additional component relative to E_{init} corresponding to the single atom diffusion barrier. (As an aside, a modified version of this formalism considers interlayer as well as lateral interactions and applies more readily for 3D NCs [54].) Both sets of interactions can be obtained from Density Functional Theory (DFT) analysis and tabulated, allowing ready determination of barriers for any local environment.

We note that the UICI formalism is readily implemented, at least for short-range pairwise interactions (with similar ease to that for the above mentioned generic formalisms). However, UICI facilitates a far more realistic description of the relevant barriers. It is also the case that the UICI formalism is readily extended to describe intermixing in more complex multicomponent systems, where the intermixing process typically involves vacancy-mediated diffusion (described by barriers for a different diverse class of local environments than for periphery diffusion).

3.2. Selected experimental examples

Far-from-equilibrium growth shapes are perhaps most clearly manifested by fractal or dendritic structures reflecting the DLA shape instability for strongly inhibited periphery diffusion. The classic example of 2D fractal epitaxial metal islands is provided by an early STM study for Au on Ru(0001) where image analysis extracted a Hausdorff dimension of $d_f = 1.72 \pm 0.07$ consistent with simulations of DLA aggregates [57]. However, the width of the “arms” of these fractal NCs far exceeds that for diffusion-mediated growth of DLA fractals incorporating a hit-and-stick mechanism. This feature was captured by a simple stochastic model where the rate of periphery diffusion was incorporated as an adjustable parameter [53]. Henceforth, we focus on fcc(111) metal homoepitaxy where not only are irregular islands observed at low T, but dramatic shape transitions occur upon increasing the deposition temperature, T. Note that in fcc(111) systems, periphery diffusion is strongly inhibited relative to terrace diffusion, but the opposite applies for fcc(100) homoepitaxy [10,54].

Figure 10a-c shows results for 2D NC shape versus T for Pt/Pt(111) [9]. Islands exhibit a fractal structure at 300 K, but a near-perfect triangular structure at 400 K, and an arrow-head form at 500 K. These shapes are distinct from the equilibrium shape which corresponds to a distorted hexagon with longer {111}-microfaceted B-steps versus {100}-microfaceted A-steps (see the inset at 500 K). These dramatic shape transitions prompted multiple modeling efforts, and also various proposals as to the

mechanism underlying the formation of triangular shapes. The latter issue was clarified in Ref. [9] where the triangles were appropriately described as a “kinetic exaggeration” of the equilibrium shapes. The lower step energy for B- vs A-steps implies weaker binding of adatoms to those B-steps, and thus a lower equilibrium density of adatoms along those B-steps. The difference in binding energies matches the difference in effective barriers for corner rounding with lower barrier for B→A that A→B. The imbalance in barriers counterbalances the imbalance in densities to ensure equal fluxes in both directions in equilibrium. However, during growth, the supersaturated edge adatom densities are more equal, and the lower B→A barrier ensures a net flux from B to A steps. This leads to the disappearance of A steps. See **Figure 11** for a schematic. Another feature of the Pt/Pt(111) system is the extreme sensitivity of growth shapes to the presence of trace amounts of CO which can, e.g., invert the direction of the triangles shown in **Figure 10b** for the CO-free case [9]. The general case with varying amounts of CO has been modeled exploiting DFT to provide key information on the relevant energetics [58].

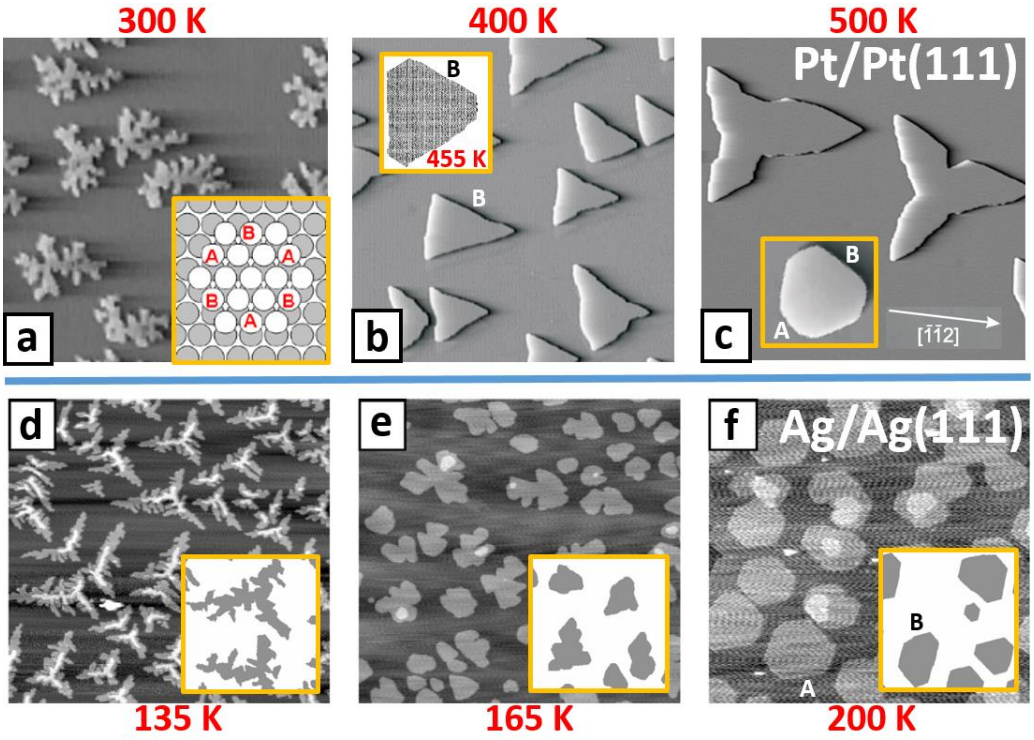

Figure 10. STM images revealing transitions in non-equilibrium island shapes of fcc(111) metal homoepitaxy. Pt/Pt(111) with no CO: (a) 78 x 78 nm^2; (b,c) 156 x 156 nm^2. Insets: (a) fcc(111) surface and step structure; (b) modeling from [58]; (c) equilibrium shape @ 700 K. (d-f) Ag/Ag(111). 300 x 300 nm^2. Insets: KMC simulation: (d) 60 x 60 nm^2; (e,f) 100 x 100 nm^2. (a-c) Refined with permission from Ref. [9]. Copyright 2004 Springer. (b) inset reprinted with permission from Ref. [58]. Copyright 2002 American Physical Society. (d-f) Refined with permission from Ref. [59]. Copyright 2005 American Physical Society.

Figure 10d-f show results for Ag/Ag(111) [59]. Islands exhibit a dendritic structure with 3-fold symmetry at 135 K, an irregular structure at 165 K, and a distorted hexagonal form at 200 K [10,59]. The equilibrium shape corresponds to a near-perfect

hexagon due to almost identical energies for A- and B-steps. The occurrence of dendrites with 3-fold symmetry at low *T* in this system, and also for Ag/Pt(111) [60] was attributed to an asymmetry in adatom diffusion from singly-coordinated sites at corners between A- and B- steps. Such atoms hop more readily to higher-coordinated sites on A-step edges than on B-step edges [9,10]. (This is the opposite of that shown in Figure 11 for Pt/Pt(111). See also Ref. [61].) Results of KMC simulation based on a model utilizing information on edge diffusion energetics from the Embedded Atom Method is shown in the insets to **Figure 10d-f** [59]. This model ignored second layer deposition and subsequent downward transport. Consequently, it failed to recover the longer A-steps observed at 200 K in STM. This deficiency was resolved by refined modeling which did include second layer deposition, but which necessarily also included a lower Ehrlich-Schwoebel barrier for downward transport at B- versus A-steps (enhancing the tendency to eliminate B-steps) [62]. Due to this step-selective interlayer transport, near triangular Ag islands could also be formed around 180 K for higher sub-monolayer coverages [62], a quite different mechanism than that for Pt/Pt(111) triangle formation. See Fig. 1 in Ref. [62].

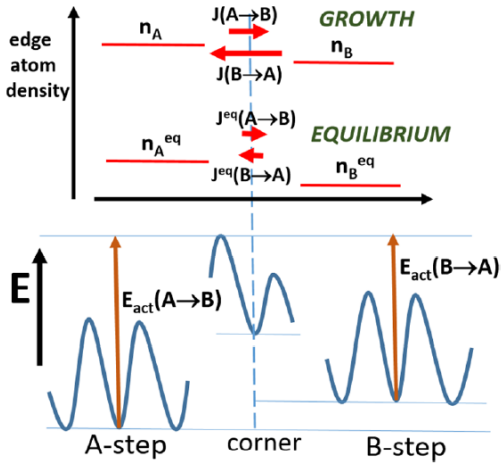

Figure 11. Schematic reflecting "kinetic exaggeration" of the somewhat distorted equilibrium hexagonal shapes towards triangular shapes for Pt/Pt(111). Reprinted with permission from Ref. [16]. Copyright 2019 American Chemical Society.

Above, data is shown for a much higher *T*-range for Pt than Ag. One could regard this as just reflecting the higher cohesive energy for Pt (5.84 eV) than Ag (2.95 eV). Regarding other fcc(111) homepitaxial systems, transitions from fractal to dendritic to triangular shapes have been observed for Al/Al(111) and described by modeling incorporating DFT input [9]. Shape transitions have also been studied for Ir/Ir(111) [63] and are quite similar to those for Pt/Pt(111).

Anisotropic surfaces on which 2D metal islands often have near-rectangular equilibrium shapes provide another example of "kinetic exaggeration". **Figure 12a** shows rectangular Ag islands formed on Ag(110) with aspect ratios in the range $\mathcal{R}$ = 3.5-5.5 at 240 K (and where $\mathcal{R}$ is higher at lower *T*) [64] significantly exceeding the equilibrium value of $\mathcal{R}_{eq} \approx 1.9$ [65]. See the **SM**. There has been extensive modeling of these non-equilibrium shapes [66]. Here, we note that the situation is analogous to that for Pt/Pt(111). Now, there is weaker binding of edge atoms on the longer (L) versus

shorter (S) edges, and a lower effective barrier for L→S versus S→L corner rounding. Thus, for supersaturated edge atom densities during deposition, the flux for L→S exceeds that for S→L producing islands with $\mathcal{R} > \mathcal{R}_{eq}$.

A similar scenario applies for Ag on NiAl(110) where there is an almost perfect match of unit cells. However, here quantum size effects induce a preference for bilayer over monolayer rectangular Ag(110) islands [67,68]. See **Figure 12b**. Nonetheless, the aspect ratio of islands formed at 200-250 K significantly exceeds the equilibrium value, which we estimate as $\mathcal{R}_{eq} \approx 2.5$. See the **SM**. Other features of interest for Ag/NiAl(110) are: (i) the presence of heterogeneous nucleation at surface defects competing with homogeneous nucleation at least at higher T [69]; and (ii) facile bilayer formation kinetics even at low $T \approx 130$ K aided by the anisotropic interactions (atoms at 1st layer kink sites which climb to the 2nd layer have only one strong in-layer bond) [67]. Note that in these anisotropic systems, NC growth shapes are primarily controlled not by anisotropic terrace diffusion, but rather by anisotropic step energies associated with anisotropic lateral interactions between adatoms.

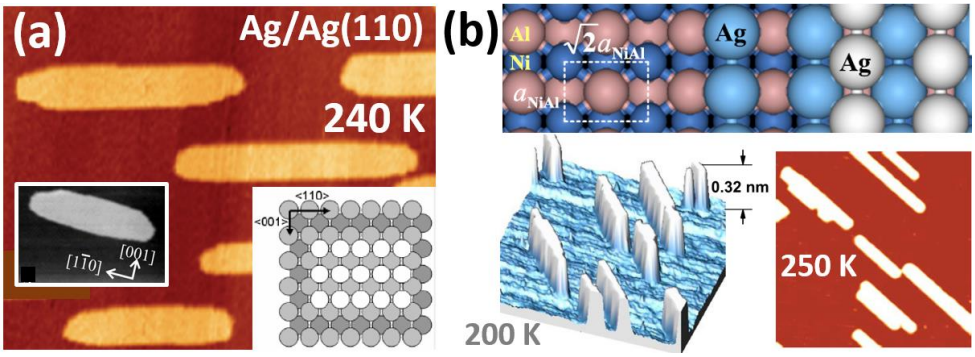

Figure 12. (a) Ag deposition on Ag(110 at 240 K. Insets show the equilibrium island shape and fcc(110) surface structure. (b) Ag deposition on NiAl(110) at 200-250 K revealing the formation of bilayer Ag(100) islands (lower panels). Surface and Ag(110) island structure (upper panel). (a) Reprinted with permission from Ref. [64]. Copyright 2013 American Physical Society. STM inset reprinted with permission from Ref. [65]. Copyright 1999 American Physical Society. (b) Reprinted with permission from Ref. [68]. Copyright 2011 National Academy of Sciences. STM inset reprinted with permission from Ref. [69]. Copyright 2010 American Physical Society.

Next, we illustrate the capabilities of the UICI modeling strategy [54-56] to treat with ab-initio level kinetics (as well as thermodynamics) Ni and Ni + Al deposition on the binary alloy substrate NiAl(110). For Ni/NiAl(110), one finds a sequence of transitions from irregular to diamond to hexagonal to distorted octagonal island shapes with increasing T [70]. See **Figure 13**. The ability for modeling to recover, and thus provide deeper understanding, of these shapes, requires precise description of periphery diffusion in this more complicated bimetallic system. **Figure 14** illustrates the conventional (solid lines) and unconventional (dashed lines) interactions in the UICI approach associated with the hopping edge atom at adsorption sites and TS, respectively, thereby mapping out the associated complete potential energy surface (PES) along the step edge. One thereby obtains insights into, e.g., anisotropic corner rounding inducing hexagonal (versus octahedral) shapes at 400 K. As an aside for

Ni/NiAl(110), analogous to Ag/NiAl(110), heterogeneous nucleation of Ni islands is dominant above 300 K.

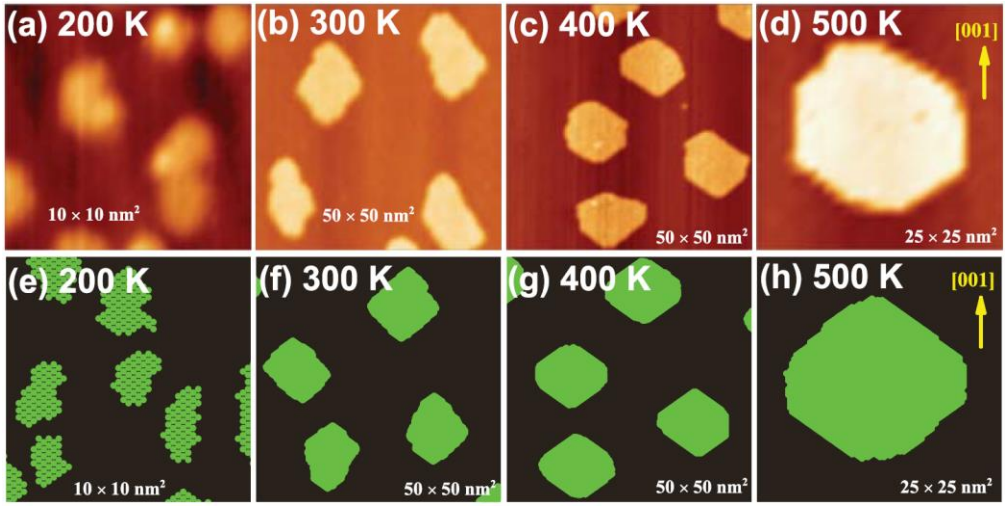

Figure 13. STM images (a-d) and associated UICI KMC simulation results (e-h) illustrating a series of transitions in growth shapes for Ni on NiAl(110). Reprinted with permission from Ref. [70]. Copyright 2011 American Institute of Physics.

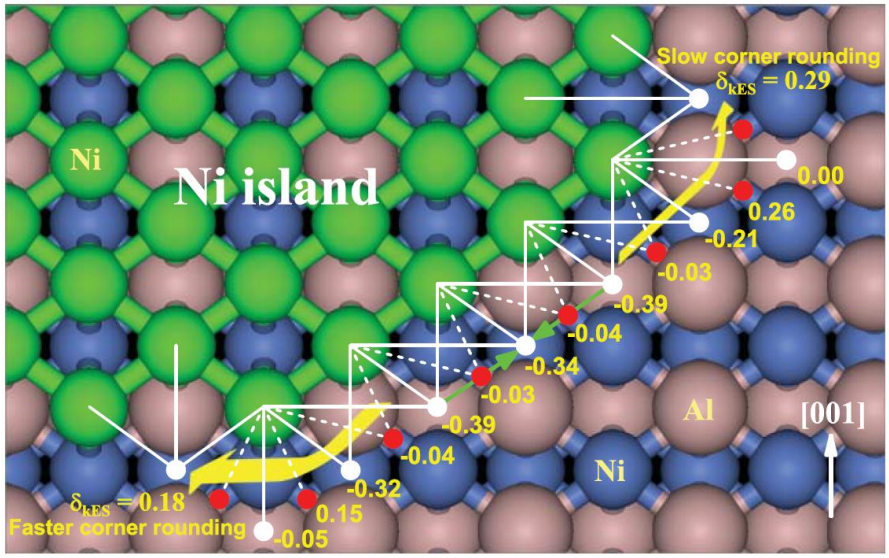

Figure 14. Schematic of the description of edge diffusion in the UICI formalism for Ni/NiAl(110) elucidating anisotropy in corner rounding. Reprinted with permission from Ref. [70]. Copyright 2011 American Institute of Physics.

Finally, extending the previous example, we consider stoichiometric co-deposition of Ni and Al on NiAl(110). At high enough T, this must result in stoichiometric self-growth of the NiAl alloy propagating the bulk structure. Thus, in the submonolayer regime, 2D islands with perfect alternating Al-Ni order would form. However, for co-deposition at around room temperature, deviations from perfect order will occur even for simultaneous co-deposition [55,71], and certainly for sequential co-deposition [68]. The latter case is illustrated in **Figure 15** where core-ring structures tend to form. Note the

robustness of the Al core in ‘Al then Ni deposition’ contrasts the fragility of the Ni core for ‘Ni then Al deposition’, where in the latter case one finds a nanoscale Kirkendall voiding type phenomenon. This behavior is readily understood by examination of associated barriers in the UICI formalism [68]. As an aside at 500 K, simultaneous co-deposition produces reasonably ordered of islands. However, for sequential Ni then Al co-deposition at 500 K, there is still significant Al ring around a predominantly Ni core, and a tendency in the intermixing part of the core to form a novel Ni_3Al ordering [55].

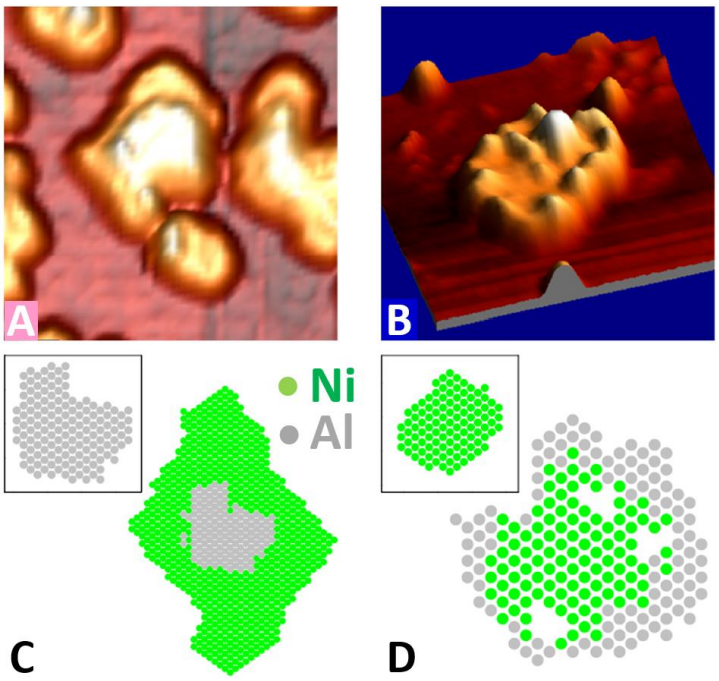

Figure 15. STM images (25 x 25 nm^2) of Al then Ni deposition (A), and Ni then Al deposition (B) at 300 K. Images from KMC simulation (C) corresponding to (A), and (D) to (B). Reprinted with permission from Ref. [68]. Copyright 2011 National Academy of Sciences.

4. 2D metal-on-metal NCs: Post-deposition coarsening

Figure 16 collates STM images and related schematics for coarsening in pristine Ag homoepitaxial systems. Ag/Ag(111) at around 300 K provides an example of classic Ostwald Ripening (OR) in 2D mediated by terrace diffusion, i.e., in the absence of an adatom attachment barrier to islands [72]. In contrast, Ag/Ag(110) below about 220 K provides an example of anomalous OR exhibiting a 1D decay mode for rectangular islands at lower T where they shrink (or grow) in length while maintaining constant width [64,65]. Contrasting both the above cases, Ag/Ag(100) at around 300 K exhibits Smoluchowski Ripening (SR) or PMC [17,73]. It is appropriate to emphasize that theoretical analysis reveals a crossover between OR and SR depending on typical island size with OR favored for larger sizes [15]. In addition for OR, the default expectation is by adatom diffusion. However, another mass transport pathway via 2D vacancies in the top layer of the substrate can potentially dominate opening additional possibilities for crossover between coarsening pathways. Indeed, for Cu/Cu(100), one finds SR at 300 K, but OR mediated by 2D vacancy diffusion at 343-413 K [74].

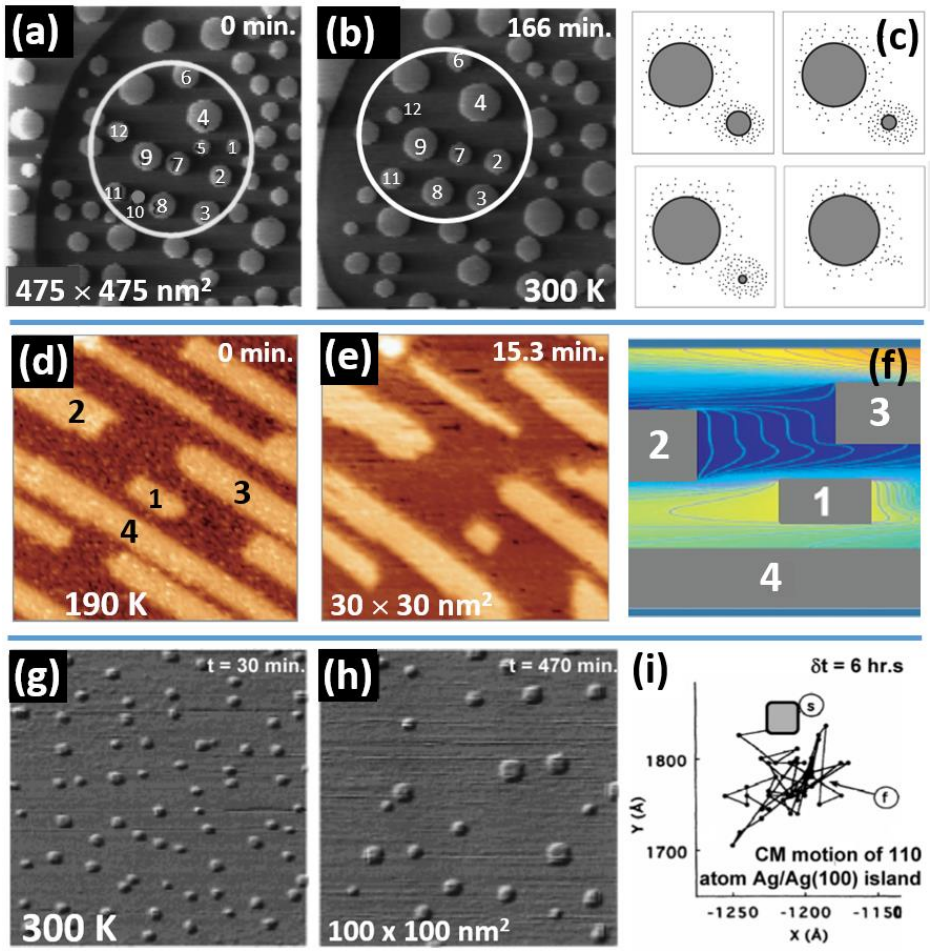

Figure 16. STM images for: (a-b) classic OR for Ag/Ag(111); (d-e) anomalous OR for Ag/Ag(110); and (g-h) SR for Ag/Ag(100). (c) Schematic of classic OR. (d) Simulation of adatom density with anisotropic attachment & diffusion. Yellow (dark blue) is 1.6 (1.3) times the equilibrium density at an extended step. (d) Diffusion path of an Ag island on Ag(100). (a-c) Refines with permission from Ref. [72]. Copyright 1999 Elsevier. (d-f) Reprinted with permission from Ref. [64]. Copyright 2013 American Physical Society. (g-i) Reprinted with permission from Ref. [15]. Copyright 2009 American Chemical Society.

4.1 OR in pristine metal homoepitaxial systems.

For Ag/Ag(111) where classic OR applies, individual islands are assumed to be locally equilibrated with chemical potentials satisfying Gibbs-Thompson condition, $\mu(R) = E_{form} + \gamma\Omega/R$ for an island of radius R. Here, E_{form} is that adatom formation energy, γ is the step energy per unit length, and Ω is the area of the surface unit cell. Thus, the equilibrium adatom density, $C_{eq}(R) = \exp[-\beta\mu(R)]$ at island edges is higher for smaller R (as indicated in **Figure 16c**) leading to a mass flow from smaller to larger islands. System evolution then follows from a Burton-Cabrera-Frank (BCF) type analysis of the steady-state diffusion equation for the adatom density exploiting the above Dirichlet boundary condition, $C = C_{eq}$, at island edges quantifying the mass flow between islands. The effective barrier for OR satisfies $E_{OR} = E_d + E_{form}$ with $E_d \approx 0.08$ eV and $E_{form} \approx 3\phi \approx$

0.66 eV for Ag/Ag(111), compatible with the value obtained by monitoring the decay of a small island inside a monolayer pit [14]. Morgenstern *et al*. [72] have shown that the above formulation can be applied to effectively describe the growth and decay rates of individual islands in **Figure 16a,b** undergoing OR. Analogous OR behavior has been observed and quantified for Cu/Cu(111) [75].

For Ag/Ag(110) which also undergoes OR, coarsening is "anomalous" at lower T [65] as noted above. Below, we let || indicate the x-direction along the rows on the {110} surface, and $\perp$ the orthogonal y-direction. Since the length of rectangular islands evolves with fixed width during OR, the classic OR assumption of equilibrated islands cannot be applied. One can instead introduce the concept of partial chemical potentials, the most relevant of which is associated varying island length for fixed width $\mu_{end} = \mu_\infty + \gamma_{end}\,\Omega/W$, where γ_{end} is the substantial step energy associated with the end of the island, and W is the island width [76]. The partial equilibrium adatom density at the end of the island is $C_{end} = \exp(-\beta\mu_{end})$. An analogous treatment applies for the chemical potential and equilibrium adatom density for the sides of the islands which have much lower step energy, γ_{side}. Then, one solves the steady-state diffusion equation with appropriate anisotropic diffusion, and incorporating general Chernov type boundary conditions

$$\pm D_{||}\,\partial C/\partial x = k_{end}(C - C_{end}) \text{ and } \pm D_{\perp}\,\partial C/\partial y = k_{side}(C - C_{side}),$$

where k denote kinetic coefficients for attachment of adatoms to step edges. In the case of no additional energetic barrier to attachment, standard BCF theory sets $k = \infty$ recovering a Dirichlet boundary condition. However, a refined BCF theory shows that for low kink density along a step, there is a high effective barrier for attachment to steps [77]. From this perspective, we set $k_{side} = 0$ as the long sides of the Ag islands have few kinks, but set $k_{end} = \infty$ since there is a high kink density at the ends of the islands and no energetic barrier to attachment. With this formalism there is no mass flux to or from the long island sides, so their width is constant. However, there is a mass flux at the ends. The form $\mu_{end} = \mu_\infty + \gamma_{end}\,\Omega/W$ means that narrower islands (with smaller W) have higher chemical potential and higher equilibrium adatom density, so mass flows from these narrower islands to wider ones. **Figure 16f** illustrates results from numerical analysis of this refined BCF formalism which recovers experimentally observed rates of island growth or shrinkage.

4.2 Chalcogen additive-enhanced OR on coinage metals

In the context of degradation of supported metal catalysts, there has long been a perception that presence of certain chemical species, X, can lead to the formation of volatile metal – X complexes which facilitate mass transport during coarsening. The same effect was observed in coinage metal homoepitaxial systems where X = O in early studies [18]. A detailed study of the effect of X = S on OR for Cu/Cu(111) revealed a remarkable acceleration of OR by two orders of magnitude for even trace amounts of S below 10 mML [78]. That study adopted the perspective that a Cu-S complex was formed on terraces, the complexes efficiently transport Cu across terraces with a net flux from smaller to larger Cu islands, and dissociate near larger island edges delivering Cu to those islands. The initial proposal was the complex was a decorated trimer, Cu_3S_3 [79]. Although Cu_3S_3 is less mobile than Cu adatoms, it also has a much lower

formation energy and thus a much higher quasi-equilibrium population on terraces, enhancing its capability as a mass carrier.

With respect to theory, Ref. [78] recognized that complex-mediated OR should be described by reaction-diffusion equations (RDE) (rather than the standard diffusion equation), where the RDE describe the formation of complexes on terraces, their diffusion across terraces, and dissociation when delivering the metal to islands. A simplified linearized version of these equations for a single complex was considered in Ref. [78]. This formulation highlighted the importance of a "reaction length", L_{rxn}, the typical length that metal adatoms diffuse before forming a complex, and the existence of different regimes of OR behavior. For example, if $L_{rxn} < L$ (the typical separation between islands), then the presence of complexes will not significantly impact OR. However, a predictive analysis for specific systems must start with the appropriate non-linear RDEs generally involving multiple complexes (which might be involved in formation of the dominant mass carrier) [80]. These non-linear RDEs can be linearized about quasi-equilibrium populations of adatoms and complexes on the surface leading to quantitative values for, e.g., reaction lengths [80-82]. This type of analysis brings into question whether Cu_3S_3 can be the dominant mass carrier (due to kinetic factors).

Additional DFT analysis explored the formation energies for a variety of Cu-S complexes including those shown in **Figure 17a**. There are multiple cases other than Cu_3S_3 with low formation energies [83]. Cu_2S_3 is the only one of these complexes which has been definitively imaged with low-*T* STM [81]. See **Figure 17b**. A necessary condition for enhanced mass transport is that the effective barrier $E_{OR} = E_d + E_{form}$ (the sum of the relevant diffusion barrier and formation energy) for complexes is below that for adatoms. This applies for CuS_2, CuS_3, Cu_2S_3, Cu_3S_3,…, (see **Table III**), but at least the latter two are ruled out based on kinetic considerations [81]. It does seem that the CuS_2 complex formed via trimolecular surface reaction Cu + S + S → CuS_2 could provide a viable pathway for enhanced surface mass transport [82].

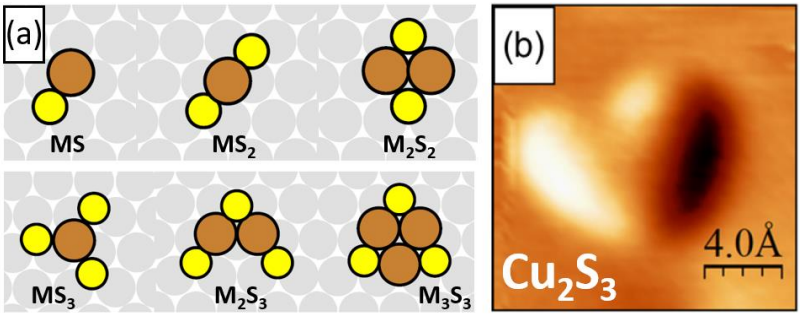

Figure 17. (a) M-S complexes analyzed by DFT; (b) low-T STM image of Cu_2S_3. Reprinted with permission from Ref. [81]. Copyright 2015 American Physical Society.

M{111}	M	MS	MS_2	M_2S_2	MS_3	M_2S_3	M_3S_3
Cu E_{form}	0.82	0.66	0.10	0.94	0.11	-0.06	0.11
Cu E_d	0.05	0.33	0.05	--	0.36	0.35	0.36
Ag E_{form}	0.62	0.59	0.01	0.86	0.13	-0.19	-0.12
Ag E_d	0.08	~0.15	~0.1	0.11	--	--	~0.3

Table III. Formation energies and diffusion barriers for M-S complexes on M{111} surfaces.

Considering other systems, S + Ag/Ag(111) with around 10 mML S exhibits a similar degree of enhancement of OR as S + Cu/Cu(111) [80], but S + Au/Au(111) exhibits much less enhancement [84]. An effort has been made to provide a comprehensive analysis of energetics for M-S complexes on {111} and {100} coinage metal surfaces, e.g., to explain the weak enhancement of coarsening observed for {100} versus {111} surfaces of Ag and Cu [83,85]. See again **Table III**.

Finally, the above analysis for S + Cu/Cu(111) was predicated on the picture proposed of complexes forming on terraces [78], which presumably anticipated a large additional barrier for complex attachment and detachment at step edges (which would contribute to E_{OR}). However, a recent theoretical analysis exploiting machine-learned potentials retaining DFT accuracy [82] suggested the existence of pathways for facile detachment of CuS_2 from S-decorated steps, where STM and DFT analysis supports such step decoration [81,82]. See **Figure 18**. The picture for S coverages where there is also a population of S adatoms on the terrace is as follows. Mobile Cu is passed from a kink site at the S-decorated step edge to pairs and triples of relatively immobile S (with $E_d(S) = 0.15$ eV) on the terrace, ultimately forming CuS_2 detached from the step edge. The overall barrier for the detachment pathway shown is 0.43 eV, well below $E_{OR}(Cu) \approx 0.87$ eV. The transition state for detachment is around images b-c in **Figure 18**, where it appears that a CuS_3 motif may play a role. Perhaps this is related to an observed scaling of the enhanced coarsening rate with the cube of S coverage [78]. A definitive analysis remains elusive.

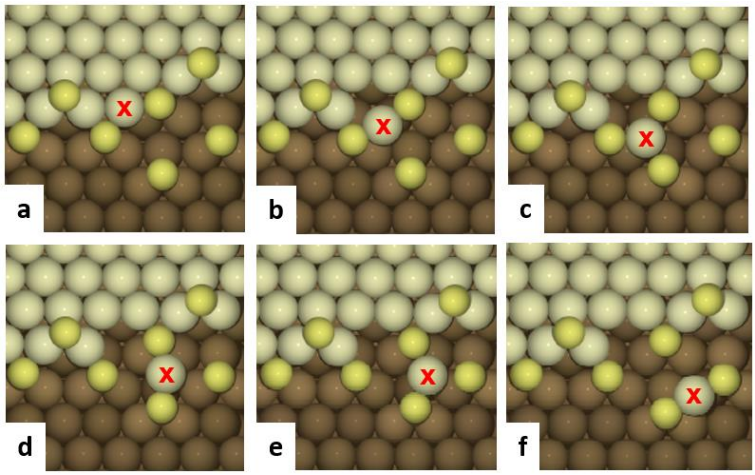

Figure 18. Facile pathway for detachment of CuS_2 from S-decorated steps in Cu(111). Reprinted with permission from Ref. [82]. Copyright 2022 American Vacuum Society.

4.3 Cluster diffusion and coalescence in SR

The discovery of significant mobility of large clusters underlying SR in metal(100) homoepitaxy was first identified for Ag [73]. A detailed characterization of the cluster diffusion coefficient, D_N versus size N (in atoms) at 295 K for N = O(10^2) was provided subsequently for both Cu and Ag [86]. It should be emphasized that this size-dependence of D_N controls the SR kinetics as determined by the Smoluchowski equation [15,16]. A simple mean-field picture of cluster diffusion mediated by random

independent hopping of edge atoms implies that $D_N \sim H\,(\delta R_{CM})^2$ where H is the total hop rate of edge atoms, and $\delta R_{CM} \sim 1/N$ is the shift in center of mass (CM) position upon each hop of an edge atom. As one has $H \sim h_e\, C_e\, N^{1/2}$, where h_e is the typical hop rate and C_e the density of edge atoms, it follows that $D_N \sim h_e\, C_e\, N^{-\beta}$ with $\beta = 3/2$. The observation of apparent deviation of $\beta \approx 1.14$-1.24 [86] from 3/2 prompted extensive theoretical analysis. However, we now argue that this was just crossover behavior between the large-size regime with $\beta = 3/2$ and distinct behavior in a moderate size regime (where the kink separation on step edges exceeded the linear cluster size) [87].

To elucidate behavior, some preliminary comments are instructive. There is a sequence of "perfect" sizes $N = N_p = L\times L$ or $L\times(L+1)$ with unique close-shell ground state square or near-square shapes. General sizes will be labeled as $N = N_p + n$ with $n = 1,2,...$, and we will find oscillatory behavior between consecutive N_p. Note that for $N = L\times(L+j)$ with $j \geq 2$, there are multiple ground-state shapes, and such N can be written as $N = N_p + n$ for suitable N_p and n. Cluster diffusion requires not just diffusion of periphery atoms, but disruption of the "core" of the cluster so that the entire cluster is translated across the surface. This requires nucleation of dimers on otherwise straight close-packed edges of clusters in their near-square ground state configuration followed by transfer of atoms to complete that new edge. See **Figure 19**.

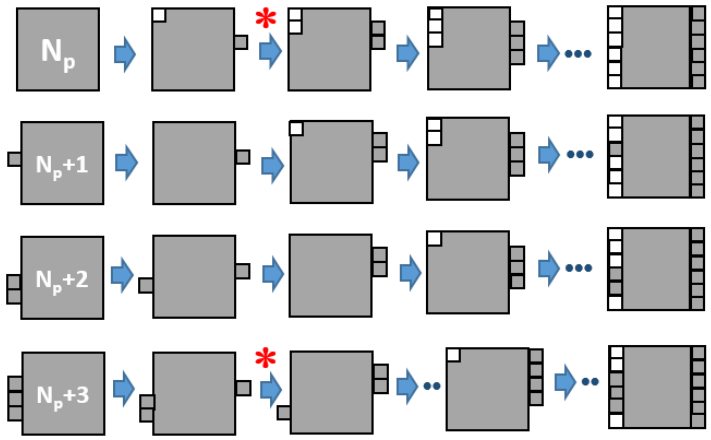

Figure 19. "Direct" pathways for cluster diffusion for sizes $N = N_p$, N_p+1, N_p+2, and N_p+3.

For quantitative analysis, we adopt a simple LG model with NN interaction of strength $\phi > 0$, barrier for diffusion along close packed edges of E_e and associated hop rate $h_e = \nu \exp(-\beta E_e)$, and a possible additional KESE barrier, δ, for kink or corner rounding. For clusters with size N_p +1 or N_p +2, the rate controlling step is extracting an atom from a kink or corner site, edge diffusion and corner rounding. Thus, the effective barrier for "facile" cluster diffusion in these cases is $E_{eff} = E_e + \phi + \delta$. For sizes N_p, N_p +3, N_p +4,…, the system passes through an energetically excited state with a single "first" edge atom on one side, with probability per site of $\exp(-\beta\phi)$. It is necessary to extract a "second" atom from a kink or corner site, and transport this atom to the first atom to nucleate a dimer before the first atom before the first atom diffuses returning the system to the initial ground state. This step is indicated by the red asterisk in Figure **19**. In these cases, one has the higher barrier of $E_{eff} = E_e + 2\phi + \delta$. Simulation results for D_N versus N in this model with $\phi = 0.24$ eV and $\delta = 0$ at 300 K are shown in **Figure 20**. (The basic

features do not change with $\delta > 0$ [87].) As might be expected, D_N for facile sizes N_p+1 and N_p+2 are highest in the moderate size regime. Perfect sizes N_p have much lower D_N than $N = N_p+1$, as anticipated in an early study [88]. However, Ref. [88] seemed to imply that $N = N_p-1$ would also be faster (which is not the case), and certainly did not anticipate the surprising result that diffusion for $N = N_p+3$ is the slowest.

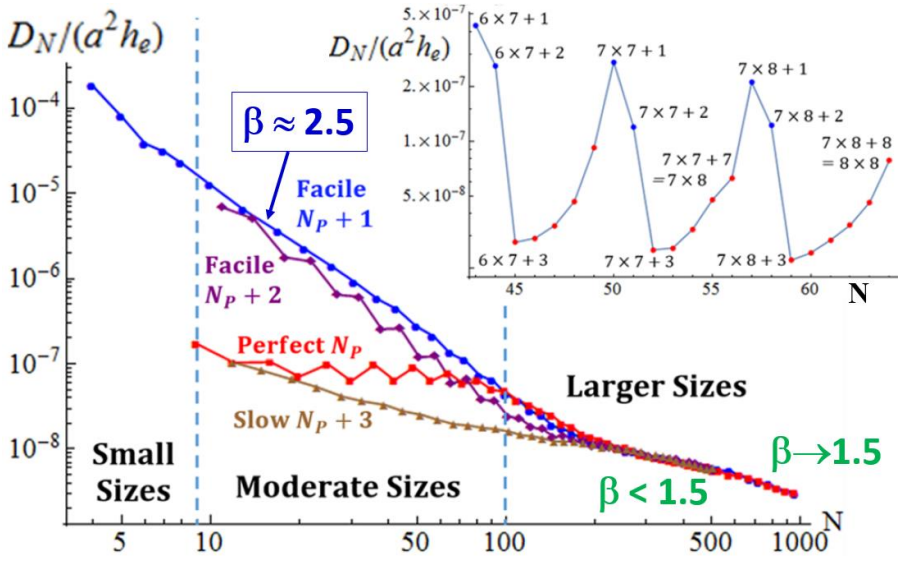

Figure 20. D_N versus N for a simple model with $\phi = 0.24$ eV and $\delta = 0$ at 300 K. Reprinted with permission from Ref. [87]. Copyright 2017 American Physical Society.

There are in fact many novel features of the results in **Figure 20** worthy of further analysis and elucidation: the rapid decrease of D_N with N for moderate $N = N_p+1$; the merging of different "branches" of behavior before N = 200; the systematic increase in D_N for $N = N_p+3$, N_p+4,… The latter is not tied to E_{eff} which adopts a single value in this range. Rather all of these features reflect entropic effects, which, e.g., smear distinctions between different branches for larger sizes. In this respect, we note that **Figure 19** is perhaps misleading showing only the most direct pathway to achieve translation of a cluster preserving its shape, and involving only ground state and first excited state configurations of the cluster. Let $\Omega_N(0)$, $\Omega_N(1)$,.. denote the degeneracy of the ground state, first excited state,… of a cluster of size N, where these quantities can be conveniently estimated exploiting "partitions of integers" concepts in number theory [87]. Here, we just make two observations. First, for facile sizes N_p+1, diffusion can occur via evolution through ground state configurations, but their degeneracy, $\Omega_N(0) \sim N^{2.6}$ increases quickly with N. However, the cluster wandering through this large phase space must repeatedly return to the first configuration shown in **Figure 19**. The return time scales like $\Omega_N(0)$, and we argue that $D_N \sim 1/\Omega_N(0)$ recovering observed behavior [87]. Second, to explain the increase in D_N for increasing $N = N_p+3$, N_p+4,… we argue that a primary factor is the decrease in $\Omega_N(0)$ with increasing N. Higher degeneracy reflects many configurations which multiple atoms shifted from corner sites, and thus many kinks, which inhibit nucleation of a dimer leading to complete of a new outer edge.

Note that most experimental data in Ref. [86] corresponded to sizes N > 100 where the distinction between facile and non-facile behavior is less clear. Again, the

values of $\beta < 1.5$ observed in experiment just correspond to a crossover regime, as is evident from **Figure 20**. Also, we note that there may be some cluster size fluctuation in experiment which would smear out fine structure in D_N versus N.

Note that cluster diffusion leads to coalescence in the SR coarsening pathway. The most prominent case is roughly corner-to-corner coalescence of near-square 2D islands. This phenomenon has been studied extensively in experiment and via modeling [15,16]. A key observation was a deviation from the prediction of a Mullins continuum prediction for the reshaping time, $\tau \sim L^{\beta^*}$, versus linear feature size L with $\beta^* = 4$ (following from a dimensional analysis of the periphery diffusion equation). Significantly lower values of β^* in the presence of a kink rounding barrier $\delta > 0$ have been observed and explained in the experimental size range [89-92], whereas $\beta^* \rightarrow 4$ for larger sizes.

5. 3D supported metal NCs: Formation and coarsening

As noted in Sec.1, early TEM studies explored metal deposition and 3D NC formation (reflecting the Volmer-Weber growth mode) on a variety of relatively weakly adhering substrates including NaCl, KCl, graphite, MoS_2, and oxides [1]. The selected metals prominently include Au and Ag, but also Pt-group metals. See Ref.s [3,93] for reviews of metals on oxides, and Ref. [94] for a recent review for metals on graphite. The extensive studies of metals on oxides, and on ultra-thin oxide films, have been motivated as these systems constitute model catalysts [3,95,96]. Another active area involves metal deposition and NC formation on supported graphene [97,98], as well as on other 2D materials such as MoS_2 [99-101].

5.1. Nucleation and growth shapes for supported 3D NCs.

There are few detailed studies of nucleation in contrast to metal-on-metal systems. However, considering metals on oxides, it is reasonable to expect that heterogeneous nucleation may often play a significant role associated with trapping at oxygen vacancy defect sites. One system which was studied extensively by experiment and modeling is Pd/MgO(100) [102-104]. A plateau exists in island density, N_{isl}, versus T up to about 565 K before a sudden drop for higher T. See **Figure 21**. This drop does not correspond to a transition from i = 1 to i > 1 which would occur at $T_{rev} \approx 680$ K corresponding to $Y = 10$ in (3) (and using $E_d = 0.2$ eV, $\phi = 1.2$ eV, $F = 10^{-3.3}$ s^{-1}, and $\nu = 10^{12.5}$ s^{-1} [104]). Instead, this behavior reflects heterogeneous nucleation where all defects are saturated with islands below 565 K. However, subsequent KMC modeling incorporating DFT energetics also highlighted the role of small cluster mobility across the surface in the nucleation process. This picture of defect mediated heterogeneous nucleation likely applies for many metals on MgO(100) [105], in particular for Ag/MgO(100) where there is a good lattice match and it was proposed that NC growth shapes are {100} epitaxially supported truncated pyramids [106,107].

We briefly note that a distinct form of nucleation and growth, which is not defect-mediated, occurs for 3D metal NCs on metal-supported graphene, where the graphene sheet generally exhibits a periodically rumpled moiré structure due to lattice mismatch with the support. In this case, directed-assembly resulting in a periodic array of NCs due to preferential nucleation in a specific region of the moiré cell. A classic example is

provided by formation of Ir NCs on Ir(111) supported graphene [98]. Effective stochastic atomistic modeling and KMC simulation was achieved accounting for the periodically modulated PES for deposited atoms on the nm scale associated with the moiré cell structure [97,108].

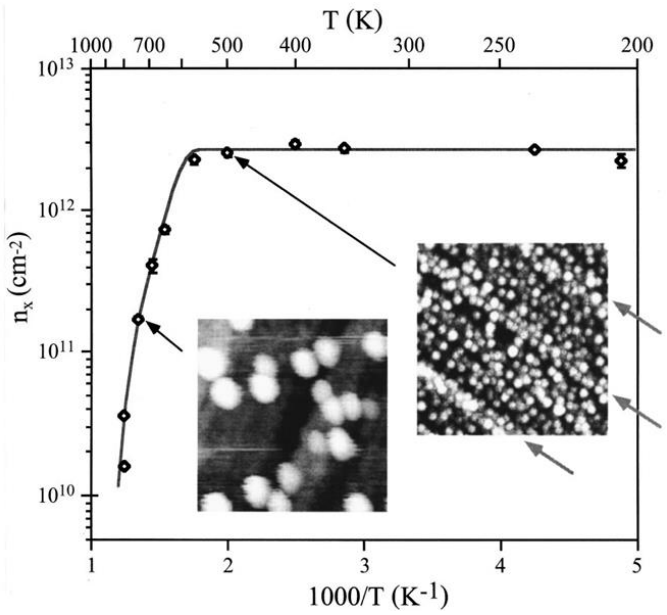

Figure 21. N_{isl} versus T for Pd/MgO(100) where insets are AFM images. Reprinted with permission from Ref. [102]. Copyright 2000 American Physical Society.

With regard to NC growth shapes, a detailed discussion can be found in the review by Henry focused on facetted polyhedral shapes [109]. NC shapes generally deviates from the equilibrium Winterbottom form, and can be regarded as being determined by the relative growth rates of different facets, with slower growing facets becoming more prominent. This picture corresponds to the geometry-based Frank's model of growth shapes, where these shapes are quantified by a so-called kinematic Wulff construction [110]. TEM imaging provides some valuable information on NC shapes, as illustrated in **Figure 22** for Au on MgO(100) [109]. Of note is the coexistence of different NC shapes, as evidenced by triangular versus rectangular footprints. These two cases corresponds to fcc{111} versus fcc{100} epitaxy, respectively. Coexistence of different NC shapes, and possibly also distinct crystal structures (as recently found for Fe on MoS_2 [101]) is expected to reflect similar energetics of these distinct structures, at least for small sizes at the onset of growth. The NCs are plausibly fluxional for small sizes and can transition between different structures. However, they presumably become locked-in to a specific structure for larger sizes during growth.

We mention another notable study of growth shapes was for 3D Pb NCs on graphite where these shapes are characterized by sharper facets than seen in equilibrium [110,111]. Also, in part for comparison with our discussion of 2D NC growth shapes in Sec. 3, we note that not just geometric growth shapes as occur in the above examples, but also dendritic structures have also been observed for 3D NCs, e.g., in the case of Au NCs on graphite [1]. Finally, we emphasize that currently there is limited

realistic and predictive atomistic-level stochastic modeling for the growth shapes of 3D NCs (in contrast to the 2D case).

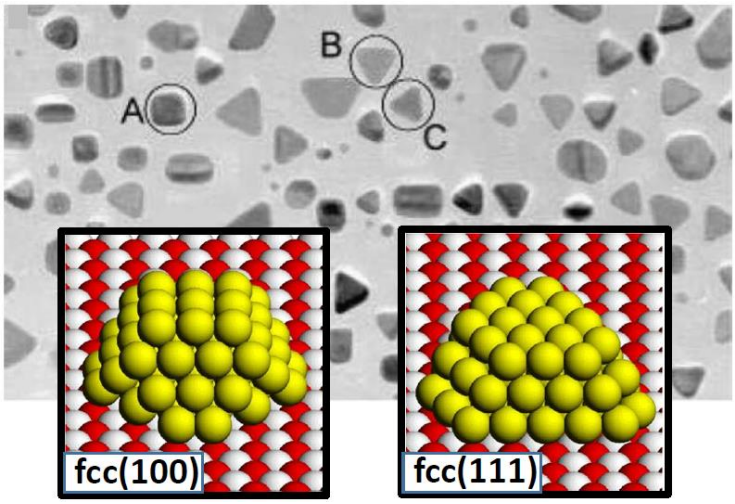

Figure 22. TEM image of Au NCs on MgO(100) [109]. A = fcc(100) epitaxy; B,C = fcc(111) epitaxy. Insets: theoretical analysis of Au NC epitaxy [107]. red = O, white = Mg, yellow = Au. Reprinted with permission from Ref. [109]. Copyright 2005 Elsevier. Insets reprinted with permission from Ref. [107]. Copyright 2000 American Institute of Physics.

5.2. OR versus SR coarsening pathways

A long-standing question for supported 3D metal NCs, particularly in the context of applications to catalysis, was whether coarsening is dominated by OR or SR (i.e., PMC). This controversy can now be resolved by examination of TEM "movies" (i.e., a sequence of images) of system evolution [112], analogous to insights extracted from STM movies for the 2D case. There have been detailed studies of OR considering in detail the size-dependence of the chemical potential for atoms in 3D NCs [113], and also assessing factors which can be utilized to inhibit OR and enhance stability of supported catalytic NCs [114]. Another recent study explored factors controlling the selection of OR versus SR [115]. We have noted previously the perception that the mass transport underling OR can be enhanced by the presence of species such as O which can create volatile complex involving the metal [116], a process which has been modeled for Pt nanoparticles in an oxygen environment [117].

Finally, paralleling the analysis in Sec. 4.3 for 2D NCs, here we consider the size-dependence of diffusion of supported 3D epitaxial NCs which controls SR kinetics. The commonly accepted mean-field picture of cluster diffusion mediated by random independent hopping of surface atoms sets $D_N \sim H\ (\delta R_{CM})^2$ with total hop rate H, and lateral CM shift per hop of $\delta R_{CM} \sim 1/N$ (analogous to 2D clusters). However, now one has $H \sim h_s\ C_e\ N^{2/3}$, with typical hop rate h_s, and surface atom density C_e, so that $D_N \sim h_s\ C_e\ N^{-\beta}$ with $\beta = 4/3$. With $h_s = \nu \exp(-\beta E_d)$ and $C_e = \exp(-\beta E_{form})$ where E_{form} is the formation energy for surface atoms, it follows that the effective barrier for cluster diffusion satisfies $E_{eff} = E_d + E_{form}$. More refined treatments include a size-dependent contribution to E_{form} associated with a Gibbs-Thompson effect [118], but it should be

noted that E_{form}, and thus the mean-field $E_{eff,}$ have well-defined finite limiting values as N $\rightarrow \infty$.

There have been few detailed atomistic level studies of 3D NC diffusion [119-121] to assess the mean-field picture. Here, we briefly describe an analysis for {100}-epitaxially supported faceted fcc NCs, as for Ag/MgO(100) [107]. This analysis reveals a fundamental breakdown of the mean-field picture (even after accounting for the feature that there are distinct adatom densities and diffusivities on different facets, and after precisely calculating E_{form} for each size [121]). The model implemented includes NN interactions of strength ϕ between metal atoms, and realistic surface diffusion kinetics with parameters selected for Ag [120]. The strength of adhesion to the substrate is selected so that the continuum equilibrium Winterbottom shape is a truncated pyramid, a discrete version of which is shown in **Figure 23b** for an NC with size N = 50 atoms [cf. Ref. [106] for Ag/Mg(100)]. KMC simulation results for D_N versus N shown in **Figure 23a** reveal an oscillatory form with local minima mostly corresponding to closed-shell sizes for truncated pyramids (sizes indicated by vertical grey lines in the figure). Determination of D_N versus T in the range 700-900 K allows extraction of the effective barrier, E_{eff}(N), for diffusion as a function of N. See **Figure 23a**. In marked contrast to the cases of 2D metal(100) homoepitaxial NC where there are just two values of E_{eff}, here the detailed oscillatory variation of E_{eff} with N tracks that of D_N with N.

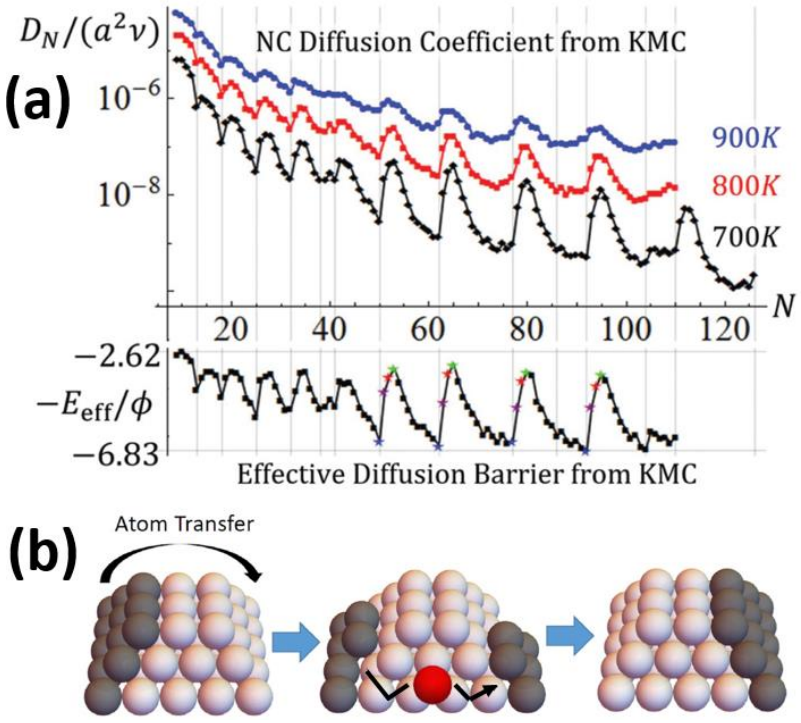

Figure 23. Diffusion of {100}-epitaxially supported truncated pyramidal fcc NCs with parameters for Ag where ϕ = 0.225 eV: (a) KMC results for D_N versus N from 700-900 K, and the associated effective barrier, E_{eff}; (b) Schematic of the underlying mechanism of disassembly & assembly of outer layers of size facets. (a) Reprinted with permission from Ref. [120]. Copyright 2019 Royal Society of Chemistry. (b) Reprinted with permission from Ref. [121]. Copyright 2023 Royal Society of Chemistry.

The above results reflect a fundamental breakdown of the mean-field picture. Rather than independent random motion of surface atoms, NC diffusion is mediated by the disassembly of the outer layer of atoms on one side facet and assembly of an outer layer on a different side facet. See **Figure 23b**. This process can be regarded as a involving the nucleation & growth of new outer layers. The energy of the system as a function of the number of atoms transferred first increases, passes through a maximum, and then decreases. Evaluation of the maximum in the energy profiles versus N tracks well with E_{eff} extracted from KMC simulation [120]. It is also the case that E_{eff} increases without bound as N increases, in contrast to the mean-field prediction. As a final aside, we note that a picture of nucleation-mediated evolution would also apply to the reshaping of non-equilibrium faceted growth shapes of 3D NCs back to their equilibrium Winterbottom shapes [16,122].

6. Conclusions

The last 30 years have seen major advances in the characterization, high-fidelity atomistic-level stochastic modeling, and understanding of the nucleation & growth of 2D epitaxial NCs, particularly for homoepitaxial systems, as well as of their often far-from-equilibrium growth shapes. Although not discussed here, this has facilitated detailed understanding of kinetic roughening and mound formation in multilayer homoepitaxial growth [9,10]. In particular, for the case of large Ehrlich-Schwoebel barriers for downward interlayer transport, multilayer mounds are built on platforms of individual submonolayer islands. A classic case is provided by multilayer fractal or dendritic wedding-cake mounds in multilayer Ag(111) homoepitaxy which are built upon submonolayer dendritic Ag islands [10]. With regard to post-deposition coarsening, submonolayer Ag/Ag(111) provides a classic example of terrace diffusion mediated OR in a well-controlled pristine system. The potential for anomalous OR even in simple homoepitaxial systems is provided by the anisotropic Ag/Ag(110) system al lower T where rectangular islands shrink or grow in length while maintaining constant width (so traditional theories of OR must be refined). The dramatic enhancement of OR in some coinage metal(111) systems due to the presence of even trace amounts of additives connects with long-held views regarding enhanced degradation of performance in catalytic nanoparticle systems. For metal(100) homoepitaxial systems, the dominance of SR rather than OR induced much interest in characterizing the size-dependence of 2D NC diffusion where comprehensive understanding was achieved only recently. Detailed analysis, incorporating high-fidelity atomistic-level stochastic modeling, is far less developed for 3D epitaxial NCs even with regard to such basic issues as elucidating growth shapes. In this respect, many opportunities await which would connect with current interest in solution-phase shape-controlled synthesis of metallic NCs [123].

Ethical approval

Not applicable.

Consent to participate

All authors have confirmed their participation. [§]Deceased. *Current address: Fritz Haber Institut der Max Planck Gesselschaft, 14195 Berlin, Germany.

Consent to publish

All authors agree to publication.

CRedit authorship contribution statement

Yong Han – Methodology, Investigation, Formal Analysis; Da-Jiang Liu – Methodology, Investigation, Formal Analysis; King C. Lai – Methodology, Investigation, Formal Analysis; Patricia A. Thiel – Conceptualization, Validation; James W. Evans – Writing – Original draft, Conceptualization, Methodology, Formal Analysis.

Declaration of competing interest

The authors declare that they have no known competing financial interest or personal relationships that could have appeared to influence the work reported in this paper.

Data availability

Data will be made available upon request.

Acknowledgements

We acknowledge fundamental contributions by former group members, Maria C. Bartelt and Maozhi Li, on nucleation theory. We thank T. Michely for providing the images in Fig. 9a-c. This work was supported by the U. S. Department of Energy (USDOE), Office of Science, Basic Energy Sciences, Division of Chemical Sciences, Geosciences, and Biological Sciences, Computational and Theoretical Chemistry (CTC) program. The work was performed at Ames National Laboratory which is operated by Iowa State University under contract No. DE-AC02-07CH11358. Some earlier work was supported by NSF grants CHE-1507223, CHE-1111500, *et al.* This research used resources of the National Energy Research Scientific Computing Center (NERSC), a DOE Office of Science User Facility supported by the Office of Science of the USDOE under Contract No. DE-AC02-05CH11231 using NERSC award BES-ERCAP0027201.

Supplementary materials

Supplementary material associated with this article can be found in the on-line version at doi:10.1018/j/susc.2024.xxxxxx

References

[1] R. Kern, G. Le Lay, J. J. Metois, Basic mechanisms in the early stages of epitaxy, in E. Kaldis (Ed.) *Current Topics in Materials Science* Vol. 3, North Holland, Amsterdam, 1979 Ch. 3, pp. 131-419.
[2] M. Zinke-Allmang, L.C. Feldman, M.H. Grabow, Clustering on surfaces, Surf. Sci. Rep. 16 (1992) 377-463.
[3] B. R. Cuenya, Synthesis and catalytic properties of metal nanoparticles: Size, shape, support, composition, and oxidation state effects, Thin Solid Films 518 (2010) 3127-3150.
[4] J. A. Venables, Rate equation approaches to thin film nucleation kinetics, Philos. Mag. 27 (1973) 697-738.
[5] J.A. Venables, Nucleation calculations in a pair-binding model, Phys. Rev. B 36 (1987) 4153-4162.
[6] C. Günther, S. Günther, E. Kopatzki, R.Q. Hwang, J. Schröder, J. Vrijmoeth, R.J. Behm, Microscopic aspects of thin metal film epitaxial growth on metallic substrates, Ber. Bunsenges. Phys. Chem. 97 (1993) 522-536.

[7] R.Q. Hwang, M.C. Bartelt, Scanning Tunneling Microscopy Studies of Metal on Metal Epitaxy, Chem. Rev. 97 (1997) 1063–1082.
[8] H. Brune, Microscopic view of epitaxial metal growth: nucleation and aggregation, Surf. Sci. Rep. 31 (1998) 121-229.
[9] T. Michely, J. Krug, *Islands, mounds, and atoms: Patterns and processes in crystal growth far from equilibrium*, Springer, Berlin, 2004.
[10] J. W. Evans, P. A. Thiel, M. C. Bartelt, Morphological evolution during epitaxial thin film growth: Formation of 2D islands and 3D mounds, Surf. Sci. Rep. 61 (2006) 1-128.
[11] Y. W. Mo, J. Kleiner, M. B. Webb, M. G. Lagally, Activation energy for surface diffusion of Si on Si(001): A scanning-tunneling-microscopy study, Phys. Rev. Lett. 66 (1991) 1998-2001.
[12] M. C. Bartelt, J. W. Evans, Scaling Analysis of Diffusion-mediated Island Growth in Surface Adsorption Processes, Phys. Rev. B. 46 (1992) 12675-12687.
[13] M.C. Bartelt, J.W. Evans, Exact Island Size Distributions for Submonolayer Deposition: Influence of Correlations between Island Size & Separation, Phys. Rev. B 54 (1996) R17359-17362.
[14] K. Morgenstern, Fast scanning tunnelling microscopy as a tool to understand changes on metal surfaces: from nanostructures to single atoms, Phys Stat Solidi B 242 (2005) 773-796.
[15] P.A. Thiel, M. Shen, D.-J. Liu, J.W. Evans, Coarsening of two-dimensional nanoclusters on metal surfaces, J. Phys. Chem. C 113 (2009) 5047-5067.
[16] K. C. Lai, Y. Han, P. Spurgeon, W. Huang, P. A. Thiel, D.-J. Liu, J. W. Evans, Reshaping, intermixing, and coarsening of metallic nanocrystals: Non-equilibrium statistical mechanical and coarse-grained modeling, Chem. Rev. 119 (2019) 6670-6768.
[17] J.-M. Wen, J. W. Evans, M. C. Bartelt, J. W. Burnett, P. A. Thiel, Coarsening mechanisms in a metal film: From cluster diffusion to vacancy ripening, Phys. Rev. Lett. 76 (1996) 652-655.
[18] P.A. Thiel, M. Shen, D.-J. Liu, J.W. Evans, Adsorbate-enhanced mass-transport on metal surfaces: oxygen and sulfur on coinage metals, J. Vac. Science Technol. A 28 (2010) 1285-1298.
[19] M. Li, M.C. Bartelt, J.W. Evans, Geometry-based simulation of submonolayer film growth, Phys. Rev. B 68 (2003) 121401-121404(R).
[20] M. Li, J.W. Evans, Geometry-based simulation (GBS) algorithms for island nucleation and growth during sub-monolayer deposition, Surf. Sci. 546 (2003) 127-148.
[21] J.D. Gunton, M. Droz Introduction to the theory of metastable and unstable states, Springer Lecture Notes in Physics Vol. 183, Springer-Verlag, Berlin, 1983.
[22] M. C. Bartelt, L. S. Perkins, J. W. Evans, Transitions in the critical size for metal(100) homoepitaxy, Surf. Sci. 344 (1995) L1193-1199.
[23] G. S. Bales and A. Zangwill, Self-consistent rate theory of submonolayer homoepitaxy with attachment/detachment kinetics, Phys. Rev. B 55 (1997) 1973-1976.
[24] C.-M. Zhang, M.C. Bartelt, J.-M. Wen, C.J. Jenks, J.W. Evans, P.A. Thiel, Submonolayer Island Formation and the Onset of Multilayer Growth during Ag/Ag(100) Homoepitaxy, Surf. Sci. 406 (1998) 178-193.
[25] C. Ratsch, P. Smilauer, A. Zangwill, D.D. Vvedensky, Submonolayer epitaxy without a critical nucleus, Surf. Sci. 329 (1995) L599-604.
[26] J. G. Amar, F. Family, Transitions in critical size in metal(100) and metal(111) homoepitaxy, Surf. Sci. 382 (1997) 170-177.
[27] M. N. Popescu, J. G. Amar, and F. Family, Self-consistent rate-equation approach to transitions in critical island size in metal(100) and metal(111) homoepitaxy, Phys. Rev. B 58 (1998) 1613-1619.
[28] G. S. Bales, D. C. Chrzan, Dynamics of irreversible island growth during submonolayer epitaxy, Phys. Rev. B 50 (1994) 6057-6067.
[29] M.C. Bartelt, A.K. Schmid, J.W. Evans, R.Q. Hwang, Island size and environment dependence of adatom capture: Cu/Co islands on Ru(0001), Phys. Rev. Lett. 81 (1998) 1901-1904.
[30] M.C. Bartelt, C.R. Stoldt, C.J. Jenks, P.A. Thiel, J.W. Evans, Adatom capture by arrays of two-dimensional Ag islands on Ag(100), Phys. Rev. B 59 (1999) 3125-3134.
[31] J.G. Amar, F. Family, Critical cluster size: Island morphology and size distribution in submonolayer epitaxial growth, Phys. Rev. Lett. 74 (1995) 2066-2069.

[32] C.R. Stoldt, C.J. Jenks, P.A. Thiel, A.M. Cadilhe, J.W. Evans, Smoluchowski Ripening of Ag Islands on Ag(100), J. Chem. Phys. 111 (1999) 5157-5166.
[33] S. Stoyanov, Nucleation theory for high and low supersaturations, in E. Kaldis (Ed.) *Current Topics in Materials Science* Vol. 3, North Holland, Amsterdam, 1979 Ch. 4, pp. 420-462.
[34] J. A. Venables, D. J. Ball, Nucleation and Growth of Rare-Gas Crystals, Proc. R. Soc. A 322 (1971) 331-354.
[35] A. Pimpinelli, T.L. Einstein, Capture-zone scaling in island nucleation: Universal fluctuation behavior, Phys. Rev. Lett. 99 (2007) 226102.
[36] M. Li, Y. Han, J.W. Evans, Comment on capture zone scaling in island nucleation: Universal fluctuation behavior, Phys. Rev. Lett. 104 (2010) 149601.
[37] Y. Han, M. Li, J.W. Evans, Scaling of capture zone area distributions for nucleation and growth of islands during submonolayer deposition, J. Chem. Phys. 145 (2016) 211911.
[38] D.D. Chambliss, K.E. Johnson, Nucleation with a critical cluster size of zero: Submonolayer Fe inclusions in Cu(100), Phys. Rev. B 50 (1994) R5012-5015.
[39] F. Shi, Y. Shim, J.G. Amar, Capture-zone areas in submonolayer nucleation: Effects of dimensionality and short-range interactions, 79 (2009) 011602.
[40] A. Pimpinelli, T. L. Einstein, Reply to comment [36], Phys. Rev. Lett. 104 (2010) 149602.
[41] T. J. Oliveira, F. D. A. Aarao Reis, Crossover in the scaling of island size and capture zone distributions, Phys. Rev. B 86 (2012) 115402.
[42] J.-S. Ferenc, Z. Neda, On the size distribution of Poisson-Voronoi cells, Physica A 385 (2007) 518-526.
[43] P. A. Mulheran, D. A. Robbie, Theory of the island and capture zone size distributions in thin film growth, Europhys. Lett. 49 (2000) 617-623.
[44] J.W. Evans, M.C. Bartelt, Nucleation, adatom capture, and island size distributions: Unified scaling analysis for submonolayer deposition, Phys. Rev. B 63 (2001) 235408.
[45] J.W. Evans, M.C. Bartelt, Island sizes and capture zone areas in submonolayer deposition: Analysis via scaling and factorization of the joint probability distribution, Phys. Rev. B 66 (2002) 235410.
[46] J. G. Amar, M. N. Popescu, and F. Family, Rate-equation approach to island capture zones and size distributions in epitaxial growth, Phys. Rev. Lett. 14 (2001) 3092-3095.
[47] A. B. Bortz, M. H. Kalos, J. L. Lebowitz, A new algorithm for Monte Carlo simulation of Ising spin systems, J. Comp. Phys. **17** (1975) 10-18.
[48] M. Li, M.C. Bartelt, J.W. Evans, Beyond-mean-field treatments of island formation during submonolayer deposition: Island size distributions for large critical sizes,
Mater. Res. Soc. Symp. Proc. Vol. 859E © 2005 Materials Research Society JJ3.1.1
[49] G. Russo, L. M. Sander, P. Smereka, Quasicontinuum Monte Carlo: A method for surface growth simulations, Phys. Rev. B 69 (2004) 121406R.
[50] J. DeVita, L. M. Sander, P. Smereka, Multiscale kinetic Monte Carlo algorithm for simulating epitaxial growth, Phys. Rev. B 72 (2005) 205421.
[51] C. Ratsch, M. F. Gyure, R. E. Caflisch, F. Gibou, M. Petersen, M. Kang, J. Garcia, and D. D. Vvedensky, Level-set method for island dynamics in epitaxial growth, Phys. Rev. B 65 (2002) 195403.
[52] G. M. Whitesides, B. Grzybowski, Self-assembly at all scales, Science 295 (2002) 2418-2421.
[53] M. C. Bartelt, J. W. Evans, Dendritic islands in metal-on-metal epitaxy I. Shape transitions and diffusion at island edges, Surf. Sci. 314 (1994) L829-L834.
[54] Y. Han, J. W. Evans, Versatile stochastic model for predictive KMC simulation of fcc metal nanostructure evolution with realistic kinetics, J. Chem. Phys, submitted (2024).
[55] Y. Han, B. Ünal, J. W. Evans, Formation of a novel ordered Ni_3Al surface structure by codeposition on NiAl(110). Phys. Rev. Lett. 108 (2012) 216102.
[56] Y. Han, D.-J. Liu, J. W. Evans, Real-time ab-initio KMC simulation of the self-assembly and sintering of bimetallic nanoclusters on fcc(100) surfaces: Au + Ag on Ag(100), Nano Lett. 14 (2014) 4646-4652.

[57] R.Q. Hwang, J. Schroeder, C. Gunther, R.J. Behm, Fractal growth of two-dimensional islands: Au on Ru(0001), Phys. Rev. Lett. 67 (1991) 3279-3282.
[58] J. Wu, E. G. Wang, K. Varga, B. G. Liu, S. T. Pantelides, Z. Zhang, Island shape selection in Pt(111) submonolayer homoepitaxy with or without CO as an adsorbate, Phys. Rev. Lett. 89 (2002) 146103.
[59] E. Cox, M. Li, P.-W. Chung, C. Ghosh, T. S. Rahman, C. J. Jenks, J. W. Evans, P. A. Thiel, Temperature dependence of island growth shapes during submonolayer deposition of Ag on Ag(111), Phys. Rev. B 71 (2005) 115414.
[60] H. Brune, H. Röder, K. Bromann, K. Kern, J. Jacobsen, P. Stoltze, K. Jacobsen, J. Nørskov, Anisotropic corner diffusion as origin for dendritic growth on hexagonal substrates, Surf. Sci. 349 (1996) L115-L122.
[61] M. Hohage, M. Bott, M. Morgenstern, Z. Zhang, T. Michely, G. Comsa, Atomic processes in low temperature Pt-dendrite growth on Pt(111), Phys. Rev. Lett. 76 (1996) 2366-2369.
[62] M. Li, P.-W. Chung, E. Cox, C. J. Jenks, P. A. Thiel, J. W. Evans, Exploration of complex multilayer film growth morphologies: STM analysis and predictive atomistic modeling for Ag on Ag(111), Phys. Rev. B 77 (2008) 033402.
[63] C. Busse, C. Polop, M. Müller, K. Albe, U. Linke, T. Michely, Stacking-fault nucleation on Ir(111), Phys. Rev. Lett. 91 (2003) 056103.
[64] Y. Han, S.M. Russell, A.R. Layson, H. Walen, C.D. Yuen, P.A. Thiel, J.W. Evans, Anisotropic coarsening: One-dimensional decay of Ag islands on Ag(110), Phys. Rev. B 87 (2013) 155420.
[65] K. Morgenstern, E. Lægsgaard, I. Stensgaard, F. Besenbacher, Transition from one-dimensional to two-dimensional island decay on an anisotropic surface, Phys. Rev. Lett. 83 (1999) 1613-1616.
[66] R. Ferrando, F. Hontinnde, A. C. Levi, Morphologies in anisotropic cluster growth: A Monte Carlo study on Ag(110), Phys. Rev. B 56 (1997) R4406-R4409.
[67] Y. Han, B. Unal, F. Qin, D. Jing, C.J. Jenks, D.-J. Liu, P.A. Thiel, J.W. Evans, Kinetics of facile bilayer island formation at low temperature: Ag/NiAl(110), Phys. Rev. Lett. 100 (2008) 116105.
[68] T. Duguet, Y. Han, C. Yuen, D. Jing, B. Ünal, J.W. Evans, P.A. Thiel, Self-assembly of metal nanostructures on binary alloy surfaces, Proc. Nat. Acad. Sci. 108 (2011) 989-994.
[69] Y. Han, B. Ünal, D. Jing, F. Qin, C.J. Jenks, D.-J. Liu, P.A. Thiel, J.W. Evans, Formation and coarsening of Ag(110) bilayer islands on NiAl(110): STM analysis and atomistic lattice-gas modeling, Phys. Rev. B 81 (2010) 115462.
[70] Y. Han, B. Ünal, D. Jing, P. A. Thiel, J. W. Evans, Temperature-dependent growth shapes of Ni nanoclusters on NiAl(110), J. Chem. Phys. 135, 084706 (2011).
[71] Y. Han, D. Jing, B. Unal, P. A. Thiel, J. W. Evans, Far-from-equilibrium film growth on alloy surfaces: Ni and Al on NiAl(110), Phys. Rev. B 84, 113414 (2011).
[72] K. Morgenstern, G. Rosenfeld, G. Comsa, Local correlation during Ostwald ripening of two-dimensional islands on Ag(111), Surf. Sci. 441 (1999) 289-300.
[73] J.-M. Wen, S.-L. Chang, J.W. Burnett, J.W. Evans, P.A. Thiel, Diffusion of large two-dimensional Ag clusters on Ag(100), Phys. Rev. Lett. 73 (1994) 2591-2594.
[74] J. B. Hannon, C. Klünker, M. Giesen, H. Ibach, N. C. Bartelt, J. C. Hamilton, Surface self-diffusion by vacancy motion: Island ripening on Cu(001), Phys. Rev. Lett. 79 (1997) 2506-2509.
[75] M. Giesen, Step and island dynamics at solid/vacuum and solid/liquid interfaces, Prog. Surf. Sci. 68 (2001) 1-153.
[76] C.-J. Wang, Y. Han, H. Walen, S.M. Russell, P.A. Thiel, J.W. Evans, Analytic formulations for one-dimensional decay of rectangular homoepitaxial islands during coarsening on anisotropic fcc(110) surfaces, Phys. Rev. B 88 (2013) 155434.
[77] D.M. Ackerman, J.W. Evans, Boundary conditions for Burton–Cabrera–Frank type step-flow models: Coarse-graining of discrete 2D deposition-diffusion equations, Multiscale Model. Simul. 9 (2011) 59-88.
[78] W. L. Ling, N. C. Bartelt, K. Pohl, J. de la Figuera, R. Q. Hwang, K. F. McCarty, Enhanced self-diffusion on Cu(111) by trace amounts of S: Chemical-reaction-limited kinetics, Phys. Rev. Lett. 93 (2004) 166101.

[79] P.J. Feibelman, Formation and diffusion of S-decorated Cu clusters on Cu(111), Phys. Rev. Lett. 85 (2000) 606-609.
[80] M. Shen, D.-J. Liu, C.J. Jenks, P.A. Thiel, J.W. Evans, Accelerated coarsening of Ag adatom islands on Ag(111) due to trace amounts of S: Mass-transport mediated by Ag–S complexes, J. Chem. Phys. 130 (2009) 094701.
[81] H. Walen, D.-J. Liu, J. Oh, H. Lim, J.W. Evans, C.M. Aikens, Y. Kim, P. A. Thiel, Cu_2S_3 complex on Cu(111) as a candidate for mass transport enhancement, Phys. Rev. B 91 (2015) 045426.
[82] D.-J. Liu, J.W. Evans, Sulfur-enhanced dynamics of coinage metal(111) surfaces: Step edges versus terraces as locations for metal-sulfur complex formation, J. Vac. Sci. Technol. A 40 (2022) 023205.
[83] J. Lee, T.L. Windus, P.A. Thiel, J.W. Evans, D.-J. Liu, Coinage metal−sulfur complexes: Stability on metal(111) surfaces and in the gas phase, J. Phys. Chem. C 123 (2019) 12954−12965.
[84] P.M. Spurgeon, D.-J. Liu, T.L. Windus, J.W. Evans, P.A. Thiel, Enhanced nanostructure dynamics on Au(111) with adsorbed sulfur due to Au-S complex formation, ChemPhysChem 22 (2021) 349-358.
[85] D.-J. Liu, P.M. Spurgeon, J. Lee, T.L. Windus, P.A. Thiel, J.W. Evans, Sulfur adsorption on coinage metal(100) surfaces: Propensity for metal–sulfur complex formation relative to (111) surfaces, Phys. Chem. Chem. Phys. 21 (2019) 26483-26491.
[86] W.W. Pai, A.K. Swan, Z. Zhang, J.F. Wendelken, Island diffusion and coarsening on metal (100) surfaces, Phys. Rev. Lett. 79 (1997) 3120-3123.
[87] K.C. Lai, D.-J. Liu, J.W. Evans, Diffusion of two-dimensional epitaxial clusters on metal (100) surfaces: Facile versus nucleation-mediated behavior and their merging for larger sizes, Phys. Rev. B 96 (2017) 235406.
[88] J. Heinonen, I. Koponen, J. Merikoski, T. Ala-Nissila, Island diffusion on metal fcc (100) surfaces, Phys. Rev. Lett. 82 (1999) 2733-2736.
[89] C. R. Stoldt, A. M. Cadilhe, C. J. Jenks, J.-M. Wen, J. W. Evans, P. A. Thiel, Evolution of far-from-equilibrium nanostructures formed by cluster-step and cluster-cluster coalescence in metal films, Phys. Rev. Lett. 81 (1998) 2950-2953.
[90] P. Jensen, N. Combe, H. Larralde, J. L. Barrat, C. Misbah, A. Pimpinelli, Kinetics of shape equilibration for two dimensional islands, Eur. Phys. J. B 11 (1999) 497-504.
[91] N. Combe, H. Larralde, Low-temperature shape relaxation of two-dimensional islands by edge diffusion, Phys. Rev. B 62 (2000) 16074-16084.
[92] D.-J. Liu, J. W. Evans, Sintering of two-dimensional nanoclusters in metal(100) homoepitaxial systems: Deviations from predictions of Mullins continuum theory, Phys. Rev. B 66 (2002) 165407.
[93] C.R. Henry, Surface studies of supported model catalysts, Surf. Sci. Rep. 31 (1998) 231-325.
[94] D. Appy, H. Lei, C.-Z. Wang, M. C. Tringides, D.-J. Liu, J. W. Evans, P. A. Thiel, Transition metals on the (0001) surface of graphite: Fundamental aspects of adsorption, diffusion, and morphology, Prog. Surf. Sci. 89 (2014) 219–238.
[95] H.J. Freund, G. Pacchioni, Oxide ultra-thin films on metals: new materials for the design of supported metal catalysts, Chem. Soc. Rev. 37 (2008) 2224–2242.
[96] C.T. Campbell, The energetics of supported metal nanoparticles: relationships to sintering rates and catalytic activity, Acc. Chem. Research 46 (2013) 1712-1719.
[97] X. Liu, Y. Han, J. W. Evans, A. Engstfeld, R. J. Behm, M. C. Tringides, M. Hupalo, H.-Q. Lin, L. Huang, K.-M. Ho, D. Appy, P. A. Thiel, C. Z. Wang, Growth morphology and properties of metals on graphene, Prog. Surf. Sci. 90 (2015) 397-443.
[98] A.T. N'Diaye, S. Bleikamp, P.J. Feibelman, T. Michely, Two-dimensional Ir cluster lattice on a graphene moiré on Ir (111), Phys. Rev. Lett. 97 (2006) 215501.
[99] A. C. Domask, K. A. Cooley, B. Kabius, M. Abraham, S. E. Mohney, Room temperature van der Waals epitaxy of metal thin films on molybdenum disulfide, Cryst. Growth Design 18 (2018) 3494-3501.
[100] D. Jing, A. Lii-Rosales, K. C. Lai, Q. Li, J. Kim, M. C. Tringides, J. W. Evans, P. A. Thiel, Far-from-equilibrium growth of metal clusters on a layered material: Cu on MoS_2, New J. Phys. 22 (2022) 053033.

[101] D. Jing, Y. Han, M. Kolmer, M.C. Tringides, J.W. Evans, Crystal structure and shape selection in the growth of 3D metallic crystallites on layered materials: Fe on MoS_2, Surf. Sci. 747 (2024) 122522.
[102] G. Haas, A. Menck, H. Brune, J. V. Barth, J. A. Venables, and K. Kern, Nucleation and growth of supported clusters at defect sites: Pd/MgO(001), Phys. Rev. B 61 (2000) 11105-11108.
[103] L. Xu, G. Henkelman, C.T. Campbell, H. Jónsson, Small Pd Clusters, up to the tetramer at least, are highly mobile on the MgO(100) surface, Phys. Rev. Lett. 95 (2005) 146103.
[104] L. Xu, C.T. Campbell, H. Jonsson, G. Henkelman, Kinetic Monte Carlo simulations of Pd deposition and island growth on MgO(100), Surf. Sci. 601 (2007) 3133-3142.
[105] J.H. Larsen, J.T. Ranney, D.E. Starr, J.E. Musgrove, and C.T. Campbell, Adsorption energetics of Ag on MgO(100), Phys. Rev. B 63 (2001) 195410.
[106] A. Barbier, G. Renaud, J. Jupille, Evolution of the cluster shape during the growth of Ag on MgO(001), Surf. Sci. 454-456 (2000) 979-983.
[107] R. Ferrando, G. Rossi, A.C. Levi, Z. Kuntová, F. Nita, A. Jelea, C. Mottet, G. Barcaro, A. Fortunelli, J. Goniakowski, Structures of metal nanoparticles adsorbed on MgO(001). I. Ag and Au, J. Chem. Phys. 130 (2009) 174702.
[108] A. Engstfeld, H. Hoster, R.J. Behm, L. Roelofs, X. Liu, C.-Z. Wang, Y. Han, J.W. Evans, Directed assembly of Ru nanoclusters on Ru(0001)-supported graphene: STM studies and atomistic modeling, Phys. Rev. B 86 (2012) 085442.
[109] C.R. Henry, Morphology of supported nanoparticles, Prog. Surf. Sci. 80 (2005) 92-116.
[110] A. Pimpinelli, J. Villain, *Physics of crystal growth*, Cambridge UP, Cambridge, 1998.
[111] J. C. Heyraud, J.J. Metois, Growth shapes of metallic crystals and roughening transitions, J. Crystal Growth 82 (1987) 269-273.
[112] T.W. Hansen, A.T. DeLaRiva, S.R. Challa, A.K. Datye, Sintering of Catalytic Nanoparticles: Particle Migration or Ostwald Ripening? Acc. Chem. Res. 46 (2013) 1720–1730.
[113] C.T. Campbell, Z. Mao, Chemical Potential of Metal Atoms in Supported Nanoparticles: Dependence upon Particle Size and Support, ACS Catal. 7 (2017) 8460-8466.
[114] J.A. Farmer, C.T. Campbell, Ceria Maintains Smaller Metal Catalyst Particles by Strong Metal-Support Bonding, Science 329 (2010) 933-936.
[115] S. Hu, W.-X. Li, Sabatier principle of metal-support interaction for design of ultrastable metal nanocatalysts, Science 374 (2021) 1360-1365.
[116] J. F. Harris, Growth and structure of supported metal catalysts particles, Int. Mater. Rev. 40 (1995) 97-115.
[117] N. Plessow, F. Abild-Pedersen, Sintering of Pt Nanoparticles via Volatile PtO_2: Simulation and Comparison with Experiments, ACS Catal. 6 (2016) 7098-7108.
[118] M.J.J. Jak, C. Konstapel, A. van Kreuningen, J. Verhoeven, J.W.M. Frenken, Scanning tunnelling microscopy study of the growth of small palladium particles on TiO2 (110), Surf. Sci. 457 (2000) 295-310.
[119] L. Li, P.N. Plessow, M. Rieger, S. Sauer, R.S. Sánchez-Carrera, A. Schaefer, F. Abild-Pedersen, Modeling the Migration of Platinum Nanoparticles on Surfaces Using a Kinetic Monte Carlo Approach, J. Phys. Chem. C 121 (2017) 4261-4269.
[120] K.C. Lai, J.W. Evans, Complex oscillatory decrease with size in diffusivity of (100)-epitaxially supported 3D fcc nanoclusters, Nanoscale 11 (2019) 17506-17516.
[121] K.C. Lai, C.T. Campbell, J.W. Evans, Size-dependent diffusion of supported metal nanoclusters: Mean-field-type treatments and beyond for faceted clusters, Nanoscale Horizons 8 (2023) 1556-1567.
[122] K.C. Lai, D.-J. Liu, W. Huang, Y. Han, J.W. Evans, Thermal shape stability of fcc metal nanocrystals synthesized with faceted nonequilibrium shapes, J. Phys. Chem. C 128 (2024) 7026−7040.
[123] Y. Xia, Y. Xiong, B. Lim, S.E. Skrabalak, Shape-controlled Synthesis of Metal Nanocrystals: Simple Chemistry meets Complex Physics? Angew. Chem., Int. Ed. 48 (2009) 60−103.